The Astrophysical Journal, 609:539–563, 2004 July 10

SUB-MILLIARCSECOND IMAGING OF QUASARS AND ACTIVE GALACTIC NUCLEI. III. KINEMATICS OF PARSEC-SCALE RADIO JETS

K. I. Kellermann, M. L. Lister,[1,2] and D. C. Homan[1,3]
National Radio Astronomy Observatory, 520 Edgemont Road, Charlottesville, VA 22903-2475;
kkellerm@nrao.edu, mlister@physics.purdue.edu, homand@denison.edu

R. C. Vermeulen
Netherlands Foundation Research in Astronomy (ASTRON), Postbus 2, NL-7990 AA Dwingeloo, Netherlands; rvermeulen@astron.nl

M. H. Cohen
Department of Astronomy, MS 105-24, California Institute of Technology, Pasadena, CA 91125; mhc@astro.caltech.edu

E. Ros and M. Kadler
Max-Planck-Institut für Radioastronomie, Auf dem Hügel 69, D-53121 Bonn, Germany; eros@mpifr-bonn.mpg.de, mkadler@mpifr-bonn.mpg.de

J. A. Zensus
Max-Planck-Institut für Radioastronomie, Auf dem Hügel 69, D-53121 Bonn, Germany; and National Radio Astronomy Observatory,
520 Edgemont Road, Charlottesville, VA 22903-2475; azensus@mpifr-bonn.mpg.de

and

Y. Y. Kovalev[1]
National Radio Astronomy Observatory, P.O. Box 2, Green Bank, WV 24944; and Astro Space Center of P. N. Lebedev Physical Institute,
Profsoyuznaya 84/32, 117997 Moscow, Russia; ykovalev@nrao.edu
Received 2004 January 6; accepted 2004 March 24

ABSTRACT

We report the results of a 15 GHz (2 cm) multiepoch Very Long Baseline Array (VLBA) program, begun in 1994 to study the outflow in radio jets ejected from quasars and active galaxies. The observed flow of 208 distinct features measured in 110 quasars, active galaxies, and BL Lac objects shows highly collimated relativistic motion with apparent transverse velocities typically between zero and about 15c, with a tail extending up to about 34c. Within individual jets, different features appear to move with a similar characteristic velocity that can represent an underlying continuous jet flow, but we also see some stationary and even apparently inward-moving features that coexist with the main features. Comparison of our observations with published data at other wavelengths suggests that there is a systematic decrease in apparent velocity with increasing wavelength, probably because the observations at different wavelengths sample different parts of the jet structure.

The observed distribution of linear velocities is not consistent with any simple ballistic model. Either there is a rather broad range of Lorentz factors, a significant difference between the velocity of the bulk relativistic flow and the pattern speed of underlying shocks, or a combination of these options. Assuming a ballistic flow, comparison of observed apparent velocities and Doppler factors computed from the timescale of flux density variations is consistent with a steep power-law distribution of intrinsic Lorentz factors, an isotropic distribution of orientations of the parent population, and intrinsic brightness temperatures about an order of magnitude below the canonical inverse Compton limit. It appears that the parent population of radio jets is not dominated by highly relativistic flows, and contrary to the assumption of simple unified models, not all sources have intrinsic speeds close to c.

Usually, the observed jet flow is in the general direction of an established jet. However, many jets show significant bends and twists, where the observed motions are nonradial but are aligned with the local jet direction, suggesting that the jet flow occurs along preexisting bent channels. In a few cases we have observed a clear change in the direction of a feature as it flows along the jet. Radio jets that are also strong gamma-ray sources detected by EGRET appear to have significantly faster speeds than the non-EGRET sources, consistent with the idea that gamma-ray sources have larger Doppler factors than non–gamma-ray sources. Sources at high redshift have systematically lower angular speeds than low-redshift jets, consistent with standard cosmologies.

Subject headings: galaxies: active — galaxies: jets — quasars: general — radio continuum: galaxies

On-line material: machine-readable tables

1. INTRODUCTION

The discovery in the mid-1960s of rapid variability in extragalactic radio sources (Sholomitskii 1965; Dent 1965; Pauliny-Toth & Kellermann 1966) appeared difficult to explain in terms of conventional synchrotron radiation theory. These early observations showed changes by as much as 25%

[1] Karl Jansky Fellow.
[2] Current address: Department of Physics, Purdue University, 525 Northwestern Avenue, West Lafayette, IN 47907.
[3] Current address: Department of Physics and Astronomy, Denison University, Granville, OH 43023.

over a few weeks, as well as significant day-to-day variations (Pauliny-Toth & Kellermann 1966). It was quickly realized (e.g., Hoyle et al. 1966) that the observed rapid variability implied such small linear dimensions that the relativistic electron population would be rapidly extinguished by inverse Compton scattering. Later, Kellermann & Pauliny-Toth (1969) put these arguments on a quantitative observational basis, showing that as a result of inverse Compton cooling, the maximum sustainable brightness temperature for an incoherent source of electron synchrotron radiation is less than 10^{12} K.

However, Woltjer (1966) and Rees (1966, 1967) pointed out that if there is relativistic bulk motion of the emitting material, since the radiation is then beamed along the direction of motion, the apparent luminosity in that direction is enhanced, while at the same time the cross section for inverse Compton scattering is reduced. Additionally, since the radiating source nearly catches up with its radiation, for a favorably positioned observer, the apparent transverse motion can exceed the speed of light. Early VLBI observations (Whitney et al. 1971; Cohen et al. 1971) showed evidence of the predicted high-velocity outflow; however, the arguments were indirect, and one had to have faith in the interpretation of the very limited radio interferometric data, which did not fully sample the source structure (e.g., Dent 1972). Subsequent higher quality VLBI observations confirmed the existence of superluminal motion in the well-collimated radio jets, found in the nuclei of many quasars and in nearby active galaxies (Cohen et al. 1977).

VLBI observations provide a direct method to investigate aspects of the formation, acceleration, and propagation of extragalactic radio jets. Early studies discussing apparent jet speeds were statistically unreliable because they were largely based on the analysis of published observations of only a few tens of sources made at different times, often at only two or three epochs, by different groups, using different antenna array configurations and different observing/data reduction strategies. The dynamic range of the images was often inadequate to identify individual features, especially for the more complex sources, and spacings in time between successive observations were frequently too long to uniquely identify and track moving jet features from epoch to epoch. Moreover, the source selection criteria for many previously published studies of superluminal motion were not well defined. A systematic study by Vermeulen (1995) of 81 sources from the flux density–limited 6 cm Caltech–Jodrell Bank Survey indicated smaller typical speeds than in earlier reports. This suggested that earlier studies preferentially tended to observe and/or report only sources in which rapid motion was detected or suspected.

In 1994 we began a systematic 15 GHz Very Long Baseline Array (VLBA) survey of relativistic outflows in a sample of over 100 quasar and active galaxy radio jets. Our motivation was to study the distributions of velocities, bending, pattern motions, accelerations, and other complexities of the jet kinematics that may exist, as well as changes in the strength and morphology of features as they propagate along the jet. These observations have provided the homogeneity, resolution, and dynamic range to reliably distinguish and identify individual components between different epochs. The central VLBA antennas provide short interferometric spacings that have allowed us to (1) track features moving for some distance down the jet where they become more diffuse and (2) observe the continuous jet rather than just the bright features that are often referred to as "components" or "blobs."

We chose 15 GHz as a compromise between achieving the best angular resolution and the better sensitivity and immunity from weather conditions found at lower frequencies. At this observing frequency the resolution of the VLBA is approximately 0.5 mas in right ascension and between 0.5 and 1 mas in declination. We therefore have sufficient angular resolution in many cases to resolve the two-dimensional jet transverse to its flow, which allows for tests of some theoretical models. In addition, individual features can often be recognized at significantly smaller separations from the origin. On the other hand, our observations are less sensitive to structure and motions of the more diffuse features located far out along the jet or within 0.5 mas of the core.

Our 15 GHz data represent a significant improvement over previous studies of superluminal motion in active galactic nuclei (AGNs). First, our sample of sources is large, and the sample membership was based on criteria other than observed superluminal motion. Second, the speeds are better determined because (1) our data are well sampled and span a longer time period and (2) our higher image resolution results in less blending of features.

In Kellermann et al. (1998, hereafter Paper I) we described the parsec-scale structure of 132 of the strongest known radio jets based on a single epoch of observation. In Zensus et al. (2002, hereafter Paper II) we discussed the structure of an additional 39 sources. Contour maps of all of our multiepoch observations are available on our Web site[4] along with kinematic and other data on each source. In this paper we discuss our multiepoch observations made through 2001 March 15 and the kinematics derived from these observations.

Some preliminary results of our program have already been published (Kellermann et al. 1999, 2000, 2003; Kellermann 2002; Ros et al. 2002; Cohen et al. 2003; Kovalev 2003; Zensus et al. 2003). We have also discussed the kinematics of several individual sources, including PKS 1345+125 (Lister et al. 2003), NGC 1052 (Vermeulen et al. 2003b), and 3C 279 (Homan et al. 2003).

In § 2 we describe our sample and source selection criteria, and in § 3 we discuss the details of our observational program. In § 4.1 we summarize the predictions of relativistic beaming models, while in § 4.2 we present the observed jet kinematics. In §§ 4.3 and 4.4 we discuss the implications of our observations for the nature of the relativistic flow. In § 4.5 we discuss the angular velocity–redshift relation, and in § 5 we summarize our results and describe our ongoing observing program.

Throughout this paper we use the following cosmological parameters: $H_0 = 70$ km s^{-1} Mpc^{-1}, $\Omega_m = 0.3$, and $\Omega_\Lambda = 0.7$.

2. SAMPLE DEFINITION

2.1. *The Full Sample*

Our original source sample (see Paper I) was based on the Kühr 1 Jy catalog (Kühr et al. 1981) as supplemented by Stickel et al. (1994). Our goal was to include all known sources in the Stickel et al. (1994) catalog that have a flat spectral index ($\alpha > -0.5$ for $S_\nu \sim \nu^\alpha$) anywhere above 500 MHz and a total flux density at 15 GHz, observed at least at one epoch, greater than 1.5 Jy for sources north of the celestial equator or greater than 2 Jy for sources between declinations -20° and the equator. Since the Stickel et al. (1994) catalog is complete only at 5 GHz, we used other measurements at 15 GHz or extrapolations from lower frequencies to augment the Kühr sample.

[4] Available at http://www.nrao.edu/2cmsurvey.

While we attempted to be complete for flat-spectrum, core-dominated sources that met our selection criteria, we also included a number of other sources of special interest as follows:

1. Six compact steep-spectrum (CSS) sources as indicated in Table 1. These sources generally have steep radio spectra and angular sizes smaller than $\sim 1''$ on the sky.
2. Four lobe-dominated sources with core components that would satisfy our criteria if they did not also have strong extended steep-spectrum structure. Two other sources, NGC 1052 (0238−084) and 3C 120 (0430+052), also have prominent double-lobe structure, but since they are core dominated on arcsecond scales at 15 GHz, they met our spectral index selection criterion.
3. Ten gigahertz-peaked spectrum (GPS) sources, some of which have two-sided jet structure (Lister et al. 2002; M. L. Lister et al. 2004, in preparation). However, many of the GPS sources we observed turned out to be merely flat-spectrum sources whose spectrum was temporarily dominated by a bright, synchrotron self-absorbed component in the jet. Our "peaked" classification in Table 1 is given only to sources that to our knowledge have always met the GPS spectral criteria given by de Vries et al. (1997). For a few sources, our classification differs from that previously published (e.g., O'Dea 1998); however, we believe that our classification is more robust (Kovalev 2004; Y. Y. Kovalev et al. 2004, in preparation).

Table 1 summarizes the properties of each source discussed in this paper. All of these sources were introduced in Papers I and II; however, 37 sources included in Papers I and II are not discussed now because they were observed only once or twice. These have subsequently been observed and will be discussed in a separate paper (E. Ros et al. 2004, in preparation). One source listed in Paper I is gravitationally lensed (0218+357), so we have chosen not to include it in our statistical discussion. Eight other sources had no detectable jet above our sensitivity limit. They are labeled as "naked cores" in Table 1, and we report no motions for these sources. Three sources, 0316+162, 1328+254, and 1328+307 reported in Papers I or II, are not discussed here as they have complex structure that we could not adequately image.

Columns (1) and (2) of Table 1 give the IAU source designation and, where appropriate, a commonly used alias. Column (3) indicates whether or not the source is a member of the representative flux density–limited sample that we describe in § 2.2. The optical classification and redshift as given mainly by Véron-Cetty & Véron (2001) are given in columns (4) and (5), respectively. In column (6) we give a radio spectral classification for each source based on RATAN-600 telescope observations of broadband instantaneous spectra from 1 to 22 GHz as described by Kovalev et al. (1999). These spectra are available on our web site. For a few sources not observed at the RATAN-600 telescope, we used published (nonsimultaneous) radio flux densities taken from the literature. We consider a radio spectrum to be "flat" if any portion of its spectrum in the range 0.6–22 GHz has a spectral index flatter than -0.5 and "steep" if the radio spectral index is steeper than -0.5 over this entire region. Column (7) shows the parsec-scale radio morphology taken from Papers I and II, column (8) shows the largest total flux density seen on any of our VLBA images, and column (9) gives an indication of whether or not the radio source is associated with a gamma-ray detection by EGRET.

2.2. *The Representative Flux Density–limited Subsample*

The full sample of sources described in the previous section is useful for investigating jet kinematics in a cross section of known AGN classes. However, in order to compare with the theoretical predictions of relativistic beaming models, a well-defined sample selected on the basis of beamed (not total) flux density is needed. Past surveys (e.g., Taylor et al. 1996; Lister 2001) have attempted to accomplish this by means of a spectral flatness criterion. However, we found that this method eliminates some lobe-dominated active galaxies such as those described in § 2.1. We also found that the extrapolated 15 GHz flux density based on nonsimultaneous lower frequency measurements was often grossly in error because of spectral curvature or variability.

We have therefore assembled a flux density–limited subsample from the full 15 GHz VLBA survey by using our measured VLBA flux densities as the main selection criterion. All sources that had a total CLEAN VLBA flux density exceeding 1.5 Jy (2 Jy for southern sources) *at any epoch since 1994* are included in this subsample. We excluded any sources that were observed on at least four occasions and never exceeded this limit. For survey sources with fewer than four VLBA epochs, we estimated the VLBA flux density at various epochs during this period using the source compactness and data from the flux density monitoring programs at the RATAN-600 radio telescope (Kovalev et al. 1999) or the University of Michigan Radio Astronomy Observatory[5] (Aller et al. 1992, 2003).

It is important to note that this subsample, although flux density–limited, is not complete; that is, there are additional compact sources that fulfill our selection criteria. This is partly due to the lack of a complete all-sky survey at 15 GHz and also to the variable nature of AGNs. We have therefore identified a list of candidate sources from other recent high-frequency radio surveys, made since our original list was compiled in 1994. These include the *WMAP* survey (Bennett et al. 2003), the VLBA calibrator survey (Beasley et al. 2002), RATAN-600 observations (Kovalev et al. 1999), and the high-frequency peaker survey (Dallacasa et al. 2000). We have made new VLBA observations of these sources in order to assemble a complete flux density–limited, core-selected sample. There are 133 sources in this complete flux density–limited sample, but so far we have multiepoch observations and derived speeds for only 71 of these sources, which we define as the representative subsample. For the purposes of the statistical analysis presented here, we consider our present subsample to be *representative* of a complete sample, since the general properties of the missing sources should not be substantially different from the whole. We have compared the 15 GHz luminosity distributions of our representative subsample and the missing sources from the full sample using a Kolmogorov-Smirnov (K-S) test and find no significant difference between the two samples.

Although our subsample selection method is somewhat complex, it is based on the directly measured compact flux density and does not use an often unreliable spectral index criterion. In addition, since the survey membership is not determined from a single "snapshot" epoch, we are not excluding potentially interesting or highly variable sources simply because they happened to be in a low state at the time of the original investigation. This increases the size of the

[5] See http://www.astro.lsa.umich.edu/obs/radiotel/umrao.html.

TABLE 1

General Source Properties

IAU Name (1)	Alias (2)	Subsample Member (3)	Optical Class (4)	Redshift (5)	Radio Spectrum (6)	Radio Morphology (7)	S_{VLBI} (Jy) (8)	EGRET ID (9)
0003−066	NRAO 005	Y	B	0.347	Flat	CJ	2.84	N
0007+106	III Zw 2, Mrk 1501	Y	G	0.0893	Flat	N	1.29	N
0016+731		Y	Q	1.781	Flat	CJ	0.98	N
0026+346		N	G[a]	0.517	Flat	CJ	0.65	N
0035+413		N	Q	1.353	Flat	CJ	0.53	N
0048−097		Y	B	...	Flat	N	1.65	N
0055+300	NGC 315	N	G	0.0165	Flat	CJ	0.82	N
0106+013		Y	Q	2.107	Flat	CJ	2.97	N
0112−017		N	Q	1.365	Flat	CJ	0.82	N
0119+041		N	Q	0.637	Flat	CJ	1.28	N
0133+476	DA 55	Y	Q	0.859	Flat	CJ	4.95	N
0149+218		N	Q	1.320	Flat	CJ	1.42	N
0153+744		N	Q	2.341	Flat	CJ	0.37	N
0202+149	4C +15.05	Y	Q[b]	0.405	Flat	CJ	2.29	Y
0202+319		Y	Q	1.466	Flat	CJ	2.27	N
0212+735		Y	Q	2.367	Flat	CJ	2.69	N
0218+357[c]		N	B[a]	0.96	Flat	CJ	0.70	N
0234+285	CTD 20	Y	Q	1.213	Flat	CJ	4.04	Y
0235+164		Y	B[d]	0.940	Flat	N	1.62	Y
0238−084	NGC 1052	Y	G	0.00490	Flat	2S	2.48	N
0316+162[e]	CTA 21	N	G	...	Peaked	CJ	0.34	N
0316+413[f]	3C 84	Y	G	0.01756	Flat	CJ	10.59	N
0333+321	NRAO 140	Y	Q	1.263	Flat	CJ	2.24	N
0336−019	CTA 26	Y	Q	0.852	Flat	CJ	3.44	Y
0355+508	NRAO 150	N	U	...	Flat	CJ	7.11	N
0415+379	3C 111	Y	G	0.0485	Steep	CJ, LD	5.98	N
0420−014		Y	Q	0.915	Flat	CJ	10.60	Y
0430+052	3C 120	Y	G	0.033	Flat	CJ	4.41	N
0440−003	NRAO 190	N	Q	0.844	Flat	CJ	1.20	Y
0454+844		N	B	...	Flat	CJ	0.34	N
0458−020		Y	Q	2.286	Flat	CJ	2.33	Y
0528+134		Y	Q	2.070	Flat	CJ	7.95	Y
0552+398	DA 193	Y	Q	2.363	Peaked	N	5.02	N
0602+673		N	Q	1.970	Flat	N	0.97	N
0605−085		Y	Q	0.872	Flat	CJ	2.80	N
0607−157		Y	Q	0.324	Flat	CJ	7.26	N
0615+820		N	Q	0.710	Flat	N	0.48	N
0642+449	OH 471	Y	Q	3.408	Peaked	CJ	4.31	N
0707+476		N	Q	1.292	Flat	CJ	0.63	N
0710+439		N	G	0.518	Peaked	2S	0.61	N
0716+714		Y	B	...	Flat	CJ	1.25	Y
0727−115		Y	Q[a]	1.591	Flat	CJ	5.30	N
0735+178		Y	B	...	Flat	CJ	1.64	Y
0736+017		Y	Q	0.191	Flat	CJ	2.58	N
0738+313	OI 363	Y	Q	0.630	Flat	CJ	2.87	N
0742+103		Y	G[a]	...	Peaked	CJ	1.50	N
0745+241		N	Q[b]	0.409	Flat	CJ	0.95	N
0748+126		Y	Q	0.889	Flat	CJ	3.25	N
0754+100		Y	B	0.266	Flat	CJ	1.83	N
0804+499		Y	Q	1.432	Flat	CJ	1.14	N
0808+019		Y	B	...	Flat	CJ	1.34	N
0814+425		Y	B	0.245	Flat	CJ	1.28	N
0823+033		Y	B	0.506	Flat	CJ	1.40	N
0829+046		Y	B	0.180	Flat	CJ	1.35	Y
0850+581		N	Q	1.322	Flat	CJ	0.61	N
0851+202	OJ 287	Y	B	0.306	Flat	CJ	4.12	Y
0859−140		N	Q	1.339	Steep	CJ, CSS	1.58	N
0906+015	4C +01.24	Y	Q	1.018	Flat	CJ	2.73	N
0917+449		N	Q	2.180	Flat	CJ	1.43	P
0923+392	4C +39.25	Y	Q	0.698	Flat	CJ	12.68	N
0945+408		Y	Q	1.252	Flat	CJ	1.59	N
0953+254		N	Q	0.712	Flat	CJ	1.31	N
1012+232	4C +23.24	N	Q	0.565	Flat	CJ	1.16	N

TABLE 1—*Continued*

IAU Name (1)	Alias (2)	Subsample Member (3)	Optical Class (4)	Redshift (5)	Radio Spectrum (6)	Radio Morphology (7)	S_{VLBI} (Jy) (8)	EGRET ID (9)
1015+359		N	Q	1.226	Flat	CJ	0.82	N
1049+215	4C +21.28	N	Q	1.300	Flat	CJ	1.45	N
1055+018	4C +01.28	Y	Q	0.888	Flat	CJ	5.30	N
1055+201	4C +20.24	N	Q	1.110	Flat	CJ	0.38	N
1101+384	Mrk 421	N	B	0.031	Flat	CJ	0.53	Y
1127−145		Y	Q	1.187	Flat	CJ	3.39	N
1128+385		N	Q	1.733	Flat	CJ	1.13	N
1155+251		N	G[a]	0.202	Flat	CJ	0.24	N
1156+295	4C +29.45	Y	Q	0.729	Flat	CJ	2.36	P
1219+285	W Comae	N	B	0.102	Flat	CJ	0.60	P
1226+023	3C 273	Y	Q	0.158	Flat	CJ	41.40	Y
1228+126	M87	Y	G	0.0044	Steep	CJ, LD	2.97	N
1253−055	3C 279	Y	Q	0.538	Flat	CJ	24.89	Y
1302−102		N	Q	0.286	Flat	CJ	0.71	N
1308+326		Y	Q	0.997	Flat	CJ	3.98	N
1323+321	4C +32.44	N	G[a]	0.370	Peaked	2S	0.65	N
1328+254[e]	3C 287	N	Q	1.055	Steep	CJ, CSS	0.09	N
1328+307[e]	3C 286	N	Q	0.846	Steep	CJ, CSS	1.23	N
1334−127		Y	Q	0.539	Flat	CJ	8.87	Y
1345+125	4C +12.50	N	G	0.121	Peaked	2S	0.99	N
1404+286	OQ 208, Mrk 668	N	G	0.077	Peaked	2S	1.20	N
1413+135		Y	B	0.247	Flat	2S	1.72	N
1424+366		N	Q	1.091	Flat	N	0.61	P
1508−055		N	Q	1.191	Steep	CJ, CSS	0.73	N
1510−089		Y	Q	0.360	Flat	CJ	2.93	Y
1532+016		N	Q	1.420	Flat	CJ	0.76	N
1546+027		Y	Q	0.412	Flat	CJ	2.83	N
1548+056	4C +05.64	Y	Q	1.422	Flat	CJ	2.92	N
1606+106	4C +10.45	Y	Q	1.226	Flat	CJ	1.93	Y
1611+343	DA 406	Y	Q	1.401	Flat	CJ	4.52	Y
1633+382	4C +38.41	Y	Q	1.807	Flat	CJ	4.28	Y
1638+398	NRAO 512	Y	Q	1.666	Flat	N	1.61	N
1641+399	3C 345	Y	Q	0.594	Flat	CJ	8.73	N
1642+690	4C +69.21	N	Q[b]	0.751	Flat	CJ	1.34	N
1652+398	Mrk 501	N	B	0.033	Flat	CJ	0.90	N
1655+077		Y	Q	0.621	Flat	CJ	2.09	N
1656+053		N	Q	0.879	Flat	CJ	0.69	N
1656+477		N	Q	1.622	Flat	CJ	1.14	N
1730−130	NRAO 530	Y	Q	0.902	Flat	CJ	10.97	Y
1749+096	4C +09.57	Y	B[d]	0.320	Flat	CJ	5.58	N
1749+701		N	B	0.770	Flat	CJ	0.79	N
1758+388		Y	Q	2.092	Peaked	CJ	1.75	N
1800+440		Y	Q	0.663	Flat	CJ	1.50	N
1803+784		Y	B[d]	0.680	Flat	CJ	2.54	N
1807+698	3C 371	N	B	0.050	Flat	CJ	1.38	N
1823+568	4C +56.27	Y	B[d]	0.663	Flat	CJ	2.31	N
1828+487	3C 380	Y	Q	0.692	Steep	CJ, CSS	2.01	N
1845+797	3C 390.3	N	G	0.057	Steep	CJ, LD	0.47	N
1901+319	3C 395	N	Q	0.635	Steep	CJ, CSS	1.35	N
1921−293		N	Q	0.352	Flat	CJ	14.39	N
1928+738	4C +73.18	Y	Q	0.303	Flat	CJ	3.92	N
1957+405	Cygnus A	Y	G	0.056	Steep	2S, LD	1.68	N
2005+403		Y	Q	1.736	Flat	CJ	2.79	N
2007+777		N	B	0.342	Flat	CJ	1.16	N
2021+317	4C +31.56	Y	U	...	Flat	CJ	2.16	N
2021+614		Y	Q[b]	0.227	Flat	CJ	2.73	N
2113+293		N	Q	1.514	Flat	CJ	0.94	N
2128−123		Y	Q	0.501	Flat	CJ	3.18	N
2131−021	4C −02.81	Y	B[d]	1.285	Flat	CJ	2.21	N
2134+004		Y	Q	1.932	Peaked	CJ	6.34	N
2136+141	OX 161	Y	Q	2.427	Flat	CJ	2.75	N
2144+092		N	Q	1.113	Flat	CJ	0.81	N
2145+067	4C +06.69	Y	Q	0.999	Flat	CJ	10.37	N
2200+420	BL Lac	Y	B	0.069	Flat	CJ	5.67	Y

TABLE 1—*Continued*

IAU Name (1)	Alias (2)	Subsample Member (3)	Optical Class (4)	Redshift (5)	Radio Spectrum (6)	Radio Morphology (7)	S_{VLBI} (Jy) (8)	EGRET ID (9)
2201+315	4C +31.63	Y	Q	0.298	Flat	CJ	3.28	N
2209+236		Y	Q[a]	1.125	Flat	CJ	1.62	Y
2223−052	3C 446	Y	Q	1.404	Flat	CJ	6.57	N
2230+114	CTA 102	Y	Q	1.037	Flat	CJ	4.86	P
2234+282	CTD 135	N	Q	0.795	Flat	CJ	1.44	N
2243−123		Y	Q	0.630	Flat	CJ	2.56	N
2251+158	3C 454.3	Y	Q	0.859	Flat	CJ	12.08	Y
2345−167		Y	Q	0.576	Flat	CJ	2.54	N

NOTES.—Col. (1): IAU name (B1950.0). Col. (2): Other name. Col. (3): Indicator for the flux density–limited subsample (see § 2). Col. (4): Optical classification according to the Véron-Cetty & Véron (2001) catalog, where Q = quasar, B = BL Lac object, G = active galaxy, and U = unidentified. Col. (5): Redshift from Véron-Cetty & Véron (2001) (the redshifts for 0026+346, 0727−115 and 1155+251 are from Paper II, that of 0202+149 is from Stickel et al. 1996, that of 0218+357 is from Lawrence 1996, that of 0754+100 is from Carangelo et al. 2003, and that of 2209+236 is from Sowards-Emmerd et al. 2003). Col. (6): Description of radio spectrum (see § 2). Col. (7): Radio morphology classification, where CJ = core jet, 2S = two-sided jet, N = naked core, LD = lobe dominated, and CSS = compact steep-spectrum object. Col. (8): Strongest 2 cm total cleaned VLBA flux density at any epoch, in Jy. Col. (9): EGRET gamma-ray source identification according to Mattox et al. (2001) and Sowards-Emmerd et al. (2003), where Y = highly probable identification, P = probable identification, N = no identification. Table 1 is also available in machine-readable form in the electronic edition of the *Astrophysical Journal*.

[a] Source not in the Véron-Cetty & Véron (2001) catalog.

[b] Source classified as a galaxy in the Véron-Cetty & Véron (2001) catalog.

[c] The source 0218+357 is a gravitationally lensed AGN that we do not include in our statistical analysis.

[d] Source classified as a quasar in the Véron-Cetty & Véron (2001) catalog.

[e] Source has large or diffuse structures that are not adequately sampled by our observations.

[f] The complex source 0316+413 (3C 84) satisfies our selection criteria but was observed as part of a separate monitoring program (Walker et al. 2000). It is included in our statistical analysis for completeness.

sample and the robustness of statistical tests on source properties. Of the 71 sources in our representative subsample, there are 53 quasars, 12 BL Lac objects, and six galaxies.

3. THE OBSERVATIONS AND ANALYSIS

Our observations were made during 29 separate observing sessions between 1994 and 2001. Typically, we obtained images of each source at three to seven epochs over this 7 yr period. Sources were usually observed at 6–18 month intervals. Those with known rapid motion were observed more frequently, while those with no observed jet or with only small observed motions were observed less often. Each observing session lasted between 8 and 24 hr. In general we tried to observe only at elevations above 10° to minimize the effect of tropospheric absorption, phase errors, and excessive ground radiation. Except for sources at low declinations, where the hour angle coverage is restricted, we observed each source once per hour for 6–8 minutes over a range of 8 hr in hour angle. In general, all 10 VLBA antennas were used for each observation, except when restricted by elevation. We rarely used less than eight antennas. Papers I and II, as well as our Web site, give logs of the observations.

Some additional observations were made in 1998 and 1999 by L. I. Gurvits et al. (2004, in preparation) as part of a different program to compare 15 GHz source structure measured with the VLBA to the 5 GHz structure measured using the Japanese *HALCA* space VLBI satellite (Hirabayashi et al. 1998). We have used these data to supplement our own as the observations were made using the same observing and data reduction procedures as used for the present program. These images are also available on our Web site.

Data reduction was done using a combination of AIPS and DIFMAP as described in Paper I. Each image was analyzed using the AIPS task JMFIT or MAXFIT to determine the relative positions of each definable feature at each epoch, and these positions were then used to calculate velocities relative to a presumed core component. We have assumed that the bright unresolved feature typically found at the end of so-called core-jet sources is the stationary core. Generally, the choice of the core is clear because of its high brightness temperature and location. However, in a few cases, the location of the core is ambiguous, particularly in some sources where the component motions appear two-sided about a centrally located core. As an aid in identifying components from one epoch to the next, we examined each image for continuity in position, flux density, and structure. Usually, this procedure is more reliable than fitting independent models to the (u, v) data at each epoch, and with the possible exception of a few isolated cases, we believe that we have correctly cross-identified features as they evolve from epoch to epoch. However, for those sources where the jet is barely resolved from the VLBA core, we fit models to the data in the (u, v)-plane in order to exploit the full interferometric resolution of the VLBA.

In Figures 1 and 2 we show the angular motion in the jets of the 120 sources for which we have been able to determine motions with three or more epochs of observation. Of these 120 sources, there are 110 sources with good-quality data and measured redshifts for which we have been able to determine the linear velocity of at least one jet feature. These comprise 13 active galaxies, 79 quasars, and 18 BL Lac objects. In all, we have been able to determine reliable values for 208 separate features found in these 110 jets.

We have determined the radial angular speed, μ, of each definable jet feature using a linear least-squares fit to the measured component positions, relative to the presumed core. Our measured values of μ are given in Table 2. In Figures 1 and 2 the slope of the line corresponds to the best-fitting least-squares fit to the speed, which is shown in column (6) of Table 2. Figure 1 shows the plots for the one-sided jets and Figure 2 the two-sided ones. For well-defined components the formal uncertainty in the relative position is small, generally less than 0.02 mas. Frequently, however, the jets have a complex brightness distribution with regions of enhanced intensity that can brighten and fade with time. In some sources,

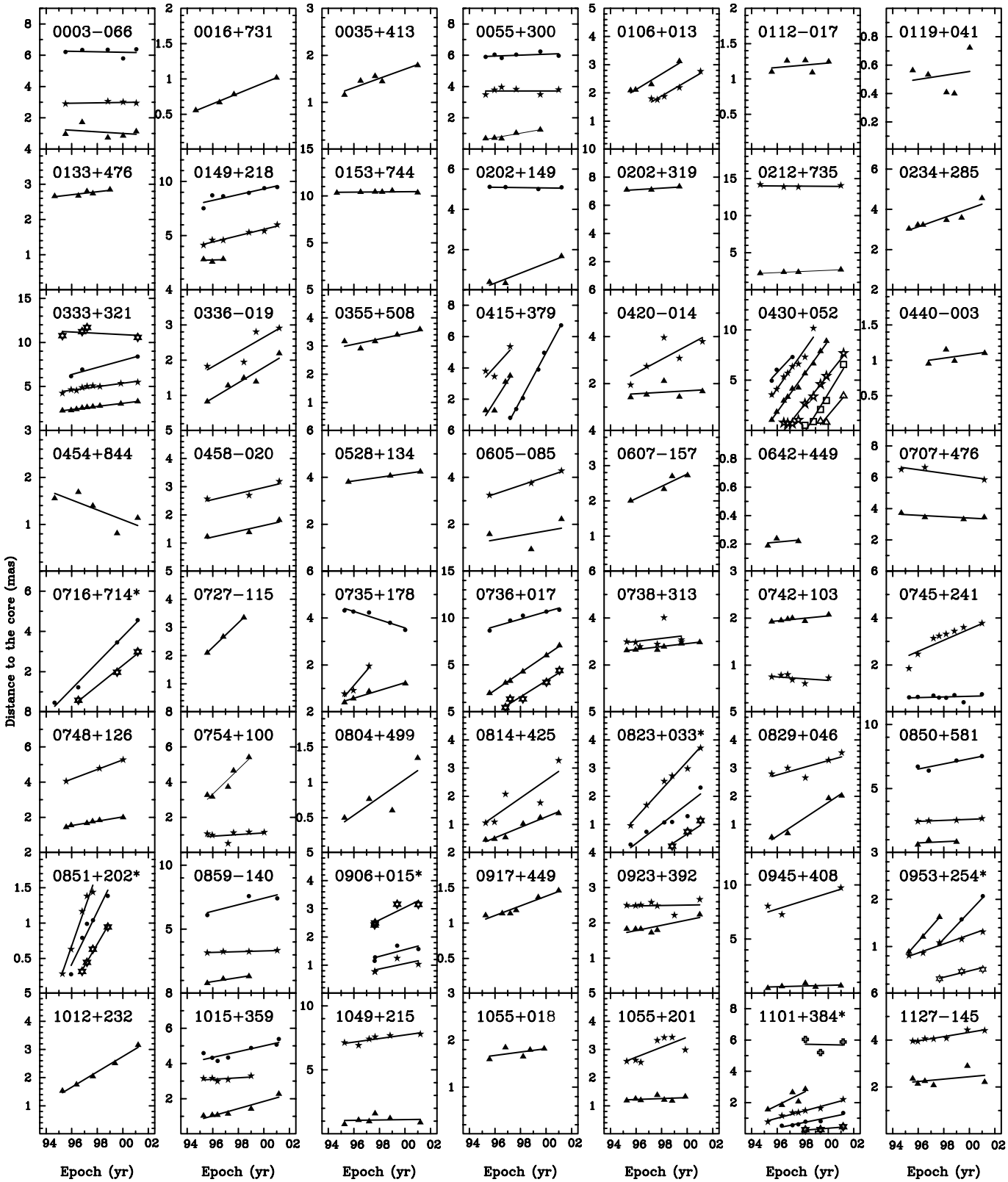

FIG. 1.—Plots showing the change in separation with time of features of one-sided jets for which we have measured a velocity from observations at three or more epochs. An asterisk denotes sources that were model fitted in the (u, v)-plane rather than in the image plane. Different symbols are used for each component as follows: B (*filled triangle*), C (*filled five-point star*), D (*filled circle*), E (*filled six-point star*), F (*cross*), G (*open five-point star*), H (*square*), I (*triangle*), J (*circle with cross*), K (*circle with dot*), L (*open circle*). The solid lines denote the best least-squares linear fit to the data, and the slope represents the proper motion, μ, tabulated in Table 2.

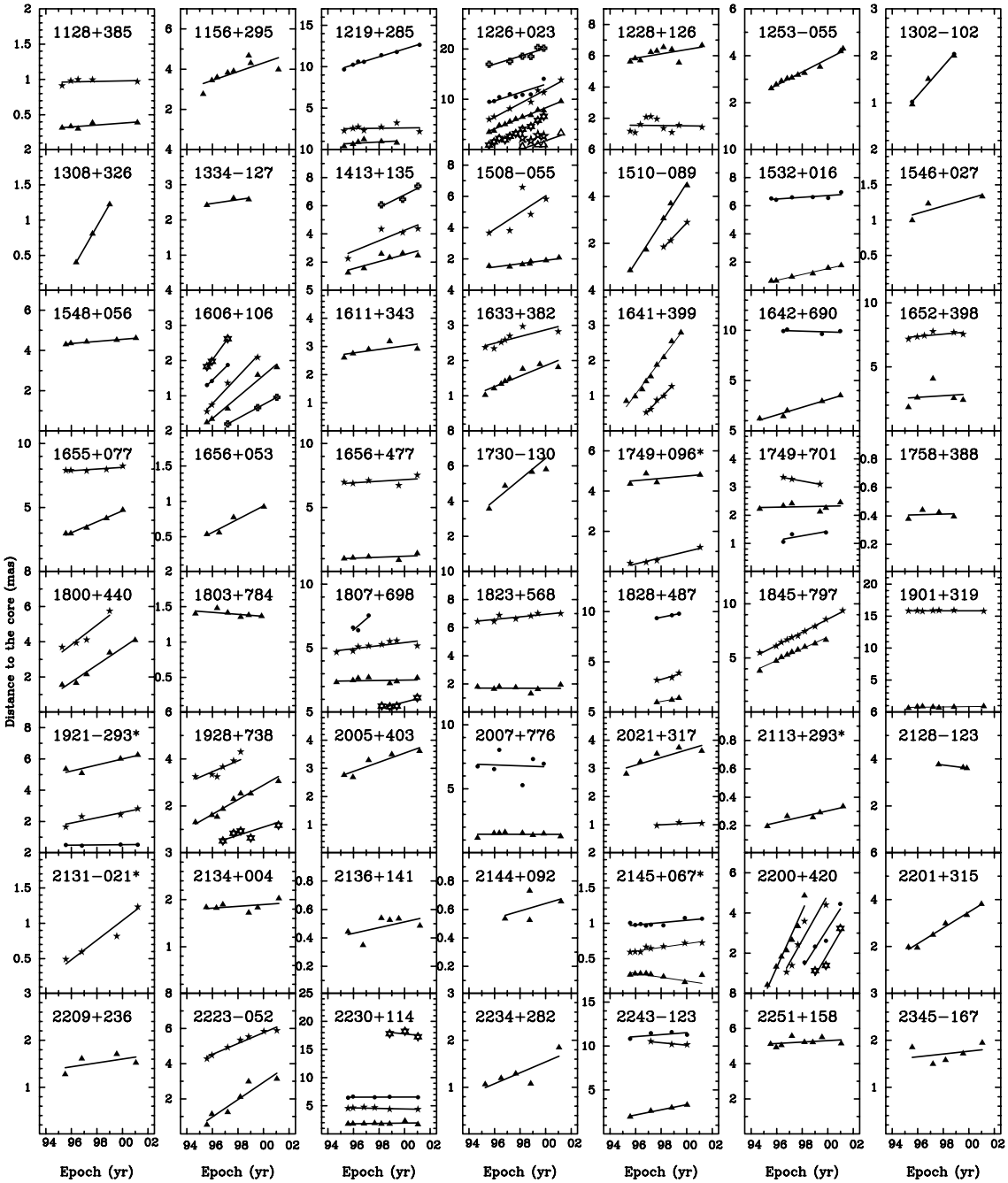

FIG. 1.—*Continued*

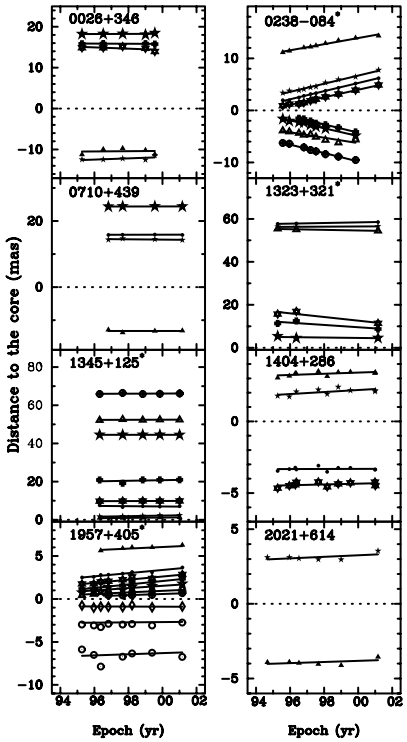

FIG. 2.—Same as Fig. 1, but for two-sided sources only. The points shown for 0238−084 (NGC 1052) are the brightest four components located on each side of the center of symmetry. No central component is visible for these sources, so the measured component positions are referred to a virtual center of symmetry as discussed by Vermeulen et al. (2003b).

instead of a well-collimated jet, there is a broad plume or more complex two-dimensional structure. Not only is the centroid of these components poorly defined, but changes in the brightness distribution with time complicate the definition of their motion. Some features appear to move, while others appear stationary. Some may break up into two or more separate features, and it is often unclear how these moving features are related to the underlying relativistic flow. In some sources, the moving features are not well resolved from each other, especially when they are close to the core. These issues all affect our ability to make a unique identification of components from epoch to epoch. In a few cases in which there are fast moving components, our observations may be too widely spaced in time to uniquely define their speed. Ambiguities exist, but we believe that most of our component identifications are robust and that component speeds are reliably determined.

We have based our error estimates of the angular velocity on the dispersion about the best-fit linear relation between the measured feature positions and time. The accuracy of each fit depends on the strength and size of the feature, the number of epochs, and the range of time covered by the observations. We note, however, that the measured dispersion of points about the best-fit line will overestimate the true scatter in component positions if there is acceleration such as observed for 3C 279 (Homan et al. 2003). Additionally, the measured radial speed may be an underestimate of the true speed if there is a significant nonradial component to the motion. However, we show in § 4.2.3 that while nonradial motions are common, the vector speeds do not differ significantly from the radial speeds, except in the case of 1548+056.

We use the following criteria to classify the quality of each measured velocity:

1. The component position is determined at four or more observations.
2. The component is a well-defined feature whose position can be unambiguously determined to a small fraction of the VLBA beamwidth.
3. The best-fitting angular speed is determined to high accuracy, defined by an uncertainty of ≤ 0.08 mas yr^{-1} or a significance[6] of $\geq 5\ \sigma$.

We then assign a "quality code" to each component motion as follows:

1. E (Excellent) denotes motions that satisfy all three of the above criteria.
2. G (Good) denotes motions that satisfy any two of the above criteria.
3. F (Fair) denotes motions that satisfy only one of the above criteria.
4. P (Poor) denotes motions that do not satisfy any of the above criteria or that the uncertainty in the fitted speed is greater than 0.15 mas yr^{-1} (except for the $\geq 5\ \sigma$ cases described above).

These codes and the measured proper motions are tabulated in Table 2.

4. DISCUSSION

4.1. *Superluminal Motion and Relativistic Beaming*

We interpret the structural changes seen in the AGNs of our sample in terms of the twin relativistic jet model of Blandford & Rees (1974). In this framework, the bulk velocity of the relativistic flow, in units of the speed of light, c, is usually denoted as β_b, and γ_b is the corresponding Lorentz factor defined by $\gamma_b = (1 - \beta_b^2)^{-1/2}$. For a jet flow at an angle θ to the observer's line of sight, the Doppler factor, δ, is given by $\delta = \gamma_b^{-1}(1 - \beta_b \cos\theta)^{-1}$.

Three important observational consequences of relativistic motion in synchrotron sources are as follows:

1. A Doppler frequency shift of the radiation, where the ratio of observed frequency ν to the emitted frequency ν_e is given by

$$\nu/\nu_e = \delta. \tag{1}$$

2. A change in the observed transverse velocity due to the apparent time compression. The apparent transverse velocity, in units of c, is given by

$$\beta_{\rm app} = \beta_p \sin\theta/\left(1 - \beta_p \cos\theta\right), \tag{2}$$

where $\beta_p = v_p/c$ is the pattern velocity. We make this distinction between pattern and bulk velocities because jet features can move with significantly different velocity than the bulk jet flow (see, e.g., Lind & Blandford 1985; Zensus et al. 1995; Vermeulen & Cohen 1994). This could be the case, for example, if the pattern motion is due to the propagation of shocks. By studying 25 core-dominated quasars selected from the literature, Vermeulen & Cohen (1994) showed that the

[6] The $\geq 5\ \sigma$ requirement is necessary to accommodate nearby sources with very high angular speed features that may have large absolute uncertainties.

TABLE 2

PROPER MOTIONS

Object (1)	Component (2)	N (3)	$\langle R \rangle$ (mas) (4)	$\langle \vartheta \rangle$ (deg) (5)	μ_r (mas yr^{-1}) (6)	$\beta_{\rm app}$ (7)	t_0 (yr) (8)	Distinct Component (9)	Rating (10)
0003−066[a]	B[b]	5	1.1	−72	−0.05 ± 0.09	−1.1 ± 2.0	...	Y	G
	C	4	3.0	−77	0.01 ± 0.02	0.3 ± 0.4	...	Y	E
	D	5	6.2	−78	−0.02 ± 0.06	−0.3 ± 1.3	...	Y	E
0016+731[a]	B[b]	4	0.8	−50	0.074 ± 0.003	5.7 ± 0.2	1987.2 ± 0.5	N	G
0026+346	B	5	10.4	−124	0.03 ± 0.23	0.9 ± 7.0	...	N	P
	C[b]	5	12.2	−129	0.15 ± 0.12	4.7 ± 3.8	...	Y	G
	E	5	14.7	56	−0.16 ± 0.12	−4.8 ± 3.6	...	Y	G
	F	4	15.8	56	−0.02 ± 0.02	−0.6 ± 0.6	...	Y	E
	G	5	18.2	59	0.02 ± 0.05	0.5 ± 1.5	...	Y	E
0035+413	B[b]	5	1.5	104	0.10 ± 0.02	6.3 ± 1.5	1982.6 ± 3.5	Y	E
0055+300	B[b]	5	0.9	−54	0.14 ± 0.03	0.16 ± 0.03	1991.0 ± 1.1	N	G
	C	6	3.7	−51	0.00 ± 0.04	0.00 ± 0.05	...	Y	E
	D	6	6.0	−51	0.03 ± 0.03	0.03 ± 0.03	...	Y	E
0106+013[a]	B[b]	4	2.4	−119	0.28 ± 0.04	23.3 ± 3.6	1988.3 ± 1.4	Y	E
	C	5	2.1	−113	0.27 ± 0.03	22.3 ± 2.7	1990.9 ± 1.0	N	G
0112−017	B[b]	5	1.2	118	0.02 ± 0.03	1.0 ± 1.8	...	Y	E
0119+041	B[b]	5	0.4	124	0.01 ± 0.04	0.5 ± 1.6	...	N	G
0133+476[a]	B[b]	5	2.7	143	0.04 ± 0.01	2.0 ± 0.7	...	Y	E
0149+218	B	3	2.8	−13	0.03 ± 0.18	1.9 ± 11.7	...	Y	P
	C	6	5.0	−22	0.29 ± 0.03	18.4 ± 1.9	1980.8 ± 1.8	Y	E
	D[b]	6	8.8	−12	0.27 ± 0.07	16.8 ± 4.6	1964.9 ± 9.0	Y	E
0153+744	B[b]	6	10.4	152	0.01 ± 0.02	1.0 ± 1.5	...	Y	E
0202+149[a]	B	3	0.8	−67	0.25 ± 0.06	6.2 ± 1.6	1994.7 ± 1.0	N	F
	D[b]	4	5.1	−59	−0.01 ± 0.01	−0.2 ± 0.3	...	Y	E
0202+319[a]	B[b]	3	7.2	−2	0.06 ± 0.03	3.9 ± 2.0	...	Y	G
0212+735[a]	B[b]	4	2.4	104	0.08 ± 0.01	7.0 ± 1.0	1966.1 ± 4.5	Y	E
	C	4	14.0	92	−0.01 ± 0.04	−1.1 ± 3.8	...	Y	E
0234+285[a]	B[b]	6	3.5	−13	0.23 ± 0.05	13.5 ± 2.9	1982.0 ± 3.4	Y	E
0238−084[a, c]	E08	7	...	...	0.68 ± 0.10	0.23 ± 0.03	1967.7 ± 4.5	Y	E
	E17	8	...	...	0.75 ± 0.12	0.25 ± 0.04	1991.4 ± 0.9	Y	E
	E20[b]	7	...	...	0.79 ± 0.12	0.26 ± 0.04	1992.7 ± 0.7	Y	E
	E23	8	...	...	0.76 ± 0.12	0.25 ± 0.04	1994.1 ± 0.5	Y	E
	W07	7	...	...	0.82 ± 0.13	0.27 ± 0.04	1984.7 ± 2.0	Y	E
	W10	7	...	...	0.72 ± 0.11	0.24 ± 0.04	1991.2 ± 1.0	Y	E
	W14	7	...	...	0.75 ± 0.12	0.25 ± 0.04	1993.4 ± 0.7	Y	E
	W16	6	...	...	0.80 ± 0.12	0.27 ± 0.04	1995.4 ± 0.4	Y	E
0316+413[a, c]	B[b]	3	...	...	0.19 ± 0.05	0.2 ± 0.1	1960.0 ± 5.0	Y	E
0333+321[a]	B[b]	9	2.7	123	0.18 ± 0.01	11.0 ± 0.5	1982.7 ± 0.7	Y	E
	C	9	4.9	126	0.20 ± 0.03	12.0 ± 1.7	1972.5 ± 3.5	Y	E
	D	3	7.2	128	0.40 ± 0.07	24.5 ± 4.5	1980.0 ± 3.3	Y	G
	E	4	11.1	131	−0.08 ± 0.13	−4.7 ± 8.1	...	N	F
0336−019[a]	B[b]	5	1.4	67	0.22 ± 0.04	10.1 ± 2.0	1991.8 ± 1.4	Y	E
	C	4	1.6	46	0.21 ± 0.08	9.7 ± 3.9	...	Y	G
0355+508	B[b]	5	3.2	46	0.09 ± 0.03	...	...	Y	E
0415+379[a]	B	4	2.3	65	1.29 ± 0.32	4.2 ± 1.0	1994.5 ± 0.5	Y	P
	C	3	4.2	70	0.90 ± 0.53	2.9 ± 1.7	...	Y	P
	D[b]	6	3.3	66	1.52 ± 0.05	4.9 ± 0.2	1996.7 ± 0.1	Y	E
0420−014[a]	B[b]	5	1.6	−163	0.03 ± 0.07	1.5 ± 3.6	...	N	G
	C	5	3.1	170	0.29 ± 0.14	14.2 ± 6.6	...	Y	G
0430+052[a]	B[b]	10	4.7	−111	1.77 ± 0.06	3.9 ± 0.1	1995.0 ± 0.1	Y	E
	C	8	6.1	−106	1.80 ± 0.19	4.0 ± 0.4	1993.7 ± 0.4	Y	E
	D	3	6.1	−110	1.36 ± 0.35	3.0 ± 0.8	1991.8 ± 1.2	Y	P
	G	9	3.0	−112	1.59 ± 0.11	3.5 ± 0.2	1996.5 ± 0.2	Y	E
	I	3	1.7	−125	1.51 ± 0.44	3.4 ± 1.0	1999.0 ± 0.4	Y	P
	H	5	2.6	−118	2.08 ± 0.24	4.6 ± 0.5	1998.2 ± 0.2	Y	E
0440−003	B[b]	4	1.1	−120	0.03 ± 0.03	1.1 ± 1.4	...	Y	E
0454+844	B[b]	5	1.3	162	−0.10 ± 0.05	...	...	Y	E
0458−020[a]	B[b]	3	1.5	−43	0.10 ± 0.04	8.9 ± 3.3	...	Y	G
	C	3	2.8	−51	0.11 ± 0.05	9.4 ± 4.1	...	Y	G
0528+134[a]	B[b]	3	4.0	23	0.077 ± 0.002	6.4 ± 0.2	1946.0 ± 1.6	Y	G
0605−085[a]	B	3	1.6	123	0.10 ± 0.21	4.5 ± 9.8	...	N	P
	C[b]	3	3.8	110	0.18 ± 0.02	8.6 ± 0.8	1977.9 ± 2.0	Y	G
0607−157[a]	B[b]	4	2.4	88	0.17 ± 0.04	3.5 ± 0.8	1984.1 ± 3.3	Y	E

TABLE 2—*Continued*

Object (1)	Component (2)	N (3)	$\langle R \rangle$ (mas) (4)	$\langle \vartheta \rangle$ (deg) (5)	μ_r (mas yr^{-1}) (6)	$\beta_{\rm app}$ (7)	t_0 (yr) (8)	Distinct Component (9)	Rating (10)
0642+449[a]	B[b]	3	0.2	92	0.01 ± 0.02	0.9 ± 2.0	...	N	F
0707+476	B[b]	4	3.5	5	−0.04 ± 0.03	−2.8 ± 1.7	...	Y	E
	C	3	6.3	24	−0.11 ± 0.05	−7.1 ± 3.3	...	Y	G
0710+439	B[b]	4	13.3	3	0.01 ± 0.13	0.2 ± 3.9	...	Y	G
	C	4	14.4	3	−0.05 ± 0.07	−1.4 ± 2.0	...	N	G
	D	4	15.8	4	0.00 ± 0.02	0.0 ± 0.5	...	Y	E
	G	4	24.4	1	0.00 ± 0.01	0.0 ± 0.3	...	Y	E
0716+714[a]	D[b]	4	2.4	14	0.65 ± 0.04	...	1994.2 ± 0.3	N	G
	E	3	1.8	11	0.51 ± 0.04	...	1995.5 ± 0.3	N	F
0727−115[a]	B[b]	3	2.7	−52	0.44 ± 0.01	31.2 ± 0.6	1990.7 ± 0.1	Y	G
0735+178[a]	B[b]	4	0.7	72	0.17 ± 0.02	...	1992.5 ± 0.7	N	G
	C	3	1.2	59	0.64 ± 0.16	...	1994.2 ± 0.5	N	P
	D	5	4.0	64	−0.18 ± 0.03	...	...	Y	E
0736+017[a]	B	6	4.2	−70	0.93 ± 0.02	11.5 ± 0.2	1993.5 ± 0.1	Y	E
	D	5	10.0	−88	0.39 ± 0.06	4.8 ± 0.8	1972.7 ± 4.1	Y	E
	E[b]	5	2.1	−68	0.85 ± 0.10	10.5 ± 1.3	1996.1 ± 0.4	Y	E
0738+313[a]	B[b]	8	2.8	179	0.06 ± 0.01	2.3 ± 0.4	1953.8 ± 8.0	Y	E
	C	7	3.1	170	0.07 ± 0.10	2.4 ± 3.8	...	N	F
0742+103[a]	B[b]	6	2.0	−5	0.03 ± 0.01	...	...	N	G
	C	6	0.7	−38	−0.02 ± 0.02	...	...	N	G
0745+241	C[b]	8	3.1	−63	0.32 ± 0.05	7.9 ± 1.3	1988.2 ± 1.6	Y	E
	D	8	0.6	−64	0.003 ± 0.022	0.1 ± 0.6	...	N	G
0748+126[a]	B[b]	6	1.7	120	0.12 ± 0.01	5.9 ± 0.5	1983.5 ± 1.1	Y	E
	C	3	4.7	111	0.274 ± 0.004	13.1 ± 0.2	1980.8 ± 0.2	Y	G
0754+100[a]	B[b]	5	4.0	15	0.70 ± 0.12	11.9 ± 2.1	1991.3 ± 1.0	Y	E
	C	6	0.9	17	0.05 ± 0.07	0.8 ± 1.2	...	N	G
0804+499[a]	B[b]	4	0.8	134	0.13 ± 0.06	8.5 ± 4.2	...	N	G
0808+019[a]	B[b]	3	0.4	−175	0.11 ± 0.01	...	1993.1 ± 0.5	N	F
	C	3	4.8	−173	−0.20 ± 0.18	...	...	Y	P
0814+425[a]	B[b]	6	0.9	90	0.18 ± 0.02	2.9 ± 0.3	1993.2 ± 0.5	N	G
	C	5	1.7	129	0.32 ± 0.11	4.9 ± 1.7	...	N	F
0823+033[a]	C	6	2.4	14	0.48 ± 0.04	14.4 ± 1.1	1993.3 ± 0.4	N	G
	D[b]	6	1.1	32	0.31 ± 0.06	9.5 ± 1.8	1994.8 ± 0.8	N	G
	E	3	0.7	32	0.41 ± 0.01	12.3 ± 0.4	1998.2 ± 0.1	N	F
0829+046[a]	B	4	1.3	66	0.30 ± 0.04	3.5 ± 0.4	1994.0 ± 0.6	N	G
	C[b]	5	3.0	66	0.13 ± 0.06	1.5 ± 0.7	...	Y	E
0850+581	B	3	0.8	174	0.05 ± 0.11	3.0 ± 7.1	...	N	P
	C[b]	4	2.5	152	0.04 ± 0.01	2.5 ± 0.5	1935.6 ± 12.5	Y	E
	D	4	7.0	151	0.20 ± 0.07	12.7 ± 4.1	1963.5 ± 11.3	Y	E
0851+202[a]	C	5	1.0	−92	0.52 ± 0.04	9.9 ± 0.9	1994.7 ± 0.2	N	G
	D[b]	5	0.9	−102	0.37 ± 0.06	7.1 ± 1.1	1994.9 ± 0.4	N	G
	E	4	0.6	−116	0.31 ± 0.02	6.0 ± 0.4	1995.7 ± 0.1	N	G
0859−140	B	3	1.1	160	0.16 ± 0.04	10.1 ± 2.8	1990.3 ± 1.9	N	F
	C[b]	4	3.2	−155	0.03 ± 0.01	1.9 ± 0.6	1889.8 ± 32.2	Y	E
	D	3	7.0	158	0.26 ± 0.15	16.3 ± 9.4	...	Y	F
0906+015[a]	C[b]	4	0.9	38	0.10 ± 0.07	5.1 ± 3.9	...	N	G
	D	4	1.4	40	0.12 ± 0.07	6.4 ± 3.5	...	N	G
	E	4	2.8	45	0.22 ± 0.07	11.8 ± 3.9	1986.3 ± 4.3	N	G
0917+449	B[b]	6	1.2	178	0.07 ± 0.01	5.8 ± 0.9	1979.8 ± 2.6	Y	E
0923+392[a]	B[b]	6	1.9	−78	0.07 ± 0.03	2.9 ± 1.0	...	Y	E
	C	7	2.5	−79	0.01 ± 0.03	0.2 ± 1.2	...	N	G
0945+408[a]	B[b]	5	0.1	−83	0.03 ± 0.04	2.0 ± 2.4	...	N	G
	C	3	8.3	119	0.37 ± 0.20	22.5 ± 12.1	...	N	P
0953+254	B	3	1.2	−108	0.31 ± 0.01	12.4 ± 0.4	1992.4 ± 0.1	N	F
	C[b]	5	1.0	−129	0.09 ± 0.01	3.5 ± 0.4	1986.1 ± 1.3	N	G
	D	3	1.6	−104	0.301 ± 0.001	12.09 ± 0.04	1994.17 ± 0.02	N	F
	E	3	0.4	−124	0.06 ± 0.02	2.4 ± 0.7	1992.0 ± 2.2	N	F
1012+232	B[b]	5	2.2	110	0.27 ± 0.02	9.0 ± 0.6	1989.9 ± 0.5	Y	E
1015+359	B[b]	6	1.3	−172	0.20 ± 0.04	12.4 ± 2.2	1991.0 ± 1.2	N	G
	C	5	3.1	−178	0.04 ± 0.04	2.6 ± 2.2	...	Y	E
	D	7	4.7	−178	0.16 ± 0.04	9.9 ± 2.5	1969.4 ± 7.1	Y	E
1049+215	B[b]	6	1.1	106	0.01 ± 0.07	0.9 ± 4.4	...	N	G
	C	6	7.4	112	0.14 ± 0.04	8.8 ± 2.6	1944.7 ± 16.1	Y	E
1055+018[a]	B[b]	5	1.7	−49	0.04 ± 0.03	1.7 ± 1.6	...	Y	E

TABLE 2—*Continued*

Object (1)	Component (2)	N (3)	$\langle R \rangle$ (mas) (4)	$\langle \vartheta \rangle$ (deg) (5)	μ_r (mas yr^{-1}) (6)	$\beta_{\rm app}$ (7)	t_0 (yr) (8)	Distinct Component (9)	Rating (10)
1055+201	B[b]	7	1.2	−10	0.02 ± 0.02	0.9 ± 1.1	...	N	G
	C	7	3.0	−5	0.18 ± 0.08	10.0 ± 4.3	...	Y	E
1101+384	B	5	2.2	−40	0.40 ± 0.15	0.8 ± 0.3	...	N	F
	C	7	1.4	−39	0.22 ± 0.02	0.46 ± 0.04	1991.5 ± 0.5	N	G
	D[b]	6	0.8	−30	0.17 ± 0.03	0.4 ± 0.1	1993.8 ± 0.7	N	G
	E	3	0.3	0	0.07 ± 0.03	0.1 ± 0.1	...	N	F
	F	3	5.7	−44	−0.02 ± 0.30	0.0 ± 0.6	...	N	P
1127−145[a]	B	6	2.3	82	0.05 ± 0.06	3.0 ± 3.5	...	Y	E
	C[b]	7	4.1	83	0.09 ± 0.01	5.4 ± 0.8	1952.5 ± 6.9	Y	E
1128+385	B[b]	5	0.3	−168	0.01 ± 0.01	1.1 ± 0.5	...	N	G
	C	5	1.0	−155	0.004 ± 0.008	0.3 ± 0.6	...	N	G
1155+251	B	3	10.2	8	0.02 ± 0.17	0.2 ± 2.2	...	N	P
	C	3	10.2	20	−0.17 ± 0.14	−2.2 ± 1.9	...	N	P
	D	3	8.0	14	0.00 ± 0.33	0.0 ± 4.3	...	N	P
	E[b]	3	3.4	21	0.03 ± 0.03	0.3 ± 0.4	...	Y	G
	F	3	4.5	−83	−0.06 ± 0.20	−0.7 ± 2.5	...	N	P
	G	3	3.0	−51	0.01 ± 0.02	0.1 ± 0.3	...	N	F
	I	3	1.2	−24	−0.03 ± 0.04	−0.4 ± 0.6	...	N	F
1156+295[a]	B[b]	8	3.8	−2	0.22 ± 0.08	8.9 ± 3.4	...	Y	G
1219+285	B	6	0.8	101	0.08 ± 0.08	0.5 ± 0.6	...	N	F
	C	7	2.5	107	0.02 ± 0.08	0.1 ± 0.5	...	Y	E
	D[b]	7	11.0	107	0.48 ± 0.03	3.2 ± 0.2	1974.5 ± 1.4	Y	E
1226+023[a]	B[b]	11	6.1	−113	1.05 ± 0.04	10.8 ± 0.5	1992.1 ± 0.3	Y	E
	C	7	9.6	−120	1.36 ± 0.11	14.1 ± 1.1	1991.3 ± 0.6	Y	E
	D	8	10.8	−119	0.83 ± 0.20	8.6 ± 2.0	1984.3 ± 3.1	Y	P
	E	10	3.3	−116	1.27 ± 0.07	13.1 ± 0.8	1995.0 ± 0.2	Y	E
	F	6	18.7	−123	0.79 ± 0.15	8.2 ± 1.6	1974.6 ± 4.6	Y	E
	G	4	2.3	−122	0.41 ± 0.39	4.2 ± 4.0	...	Y	P
	I	4	1.4	−122	0.88 ± 0.32	9.1 ± 3.3	...	Y	P
1228+126[a]	B	9	6.0	−76	0.14 ± 0.07	0.04 ± 0.02	...	N	G
	C[b]	10	1.5	−78	−0.01 ± 0.08	0.00 ± 0.02	...	N	G
1253−055[a]	B[b]	10	3.3	−116	0.28 ± 0.01	8.9 ± 0.4	1986.2 ± 0.6	Y	E
1302−102	B[b]	3	1.5	30	0.31 ± 0.05	5.6 ± 0.9	1992.3 ± 0.8	N	F
1308+326[a]	B[b]	3	0.8	−80	0.313 ± 0.002	16.3 ± 0.1	1995.08 ± 0.01	Y	G
1323+321	C	3	56.4	−51	0.04 ± 0.03	0.9 ± 0.8	...	N	F
	D	3	58.0	−50	0.142 ± 0.001	3.25 ± 0.02	1588.5 ± 1.4	N	F
	E	3	14.6	−46	−0.86 ± 0.35	−19.7 ± 8.0	...	N	P
	F	3	10.8	−41	−0.54 ± 0.28	−12.3 ± 6.5	...	N	P
	G	3	4.8	−35	−0.10 ± 0.12	−2.2 ± 2.8	...	N	P
	I[b]	3	55.0	−50	−0.15 ± 0.03	−3.4 ± 0.7	...	N	F
1334−127[a]	B[b]	3	2.5	156	0.05 ± 0.03	1.7 ± 1.0	...	N	F
1345+125	B	5	1.1	168	0.09 ± 0.02	0.7 ± 0.2	1986.8 ± 3.2	Y	E
	C	5	2.0	164	0.15 ± 0.02	1.2 ± 0.1	1985.7 ± 1.5	Y	E
	D	5	7.1	171	−0.07 ± 0.09	−0.6 ± 0.7	...	Y	G
	E[b]	5	9.8	162	0.03 ± 0.01	0.2 ± 0.1	...	Y	E
	F	5	20.6	156	0.16 ± 0.23	1.3 ± 1.9	...	Y	P
	G	5	44.5	155	−0.01 ± 0.01	−0.06 ± 0.05	...	Y	E
	I	5	52.4	161	0.02 ± 0.05	0.1 ± 0.4	...	Y	E
	J	5	66.1	177	0.03 ± 0.08	0.2 ± 0.6	...	Y	E
1404+286	B[b]	10	3.3	53	0.04 ± 0.02	0.2 ± 0.1	...	Y	E
	C	9	2.0	62	0.06 ± 0.03	0.3 ± 0.2	...	Y	E
	D	10	3.3	−127	0.00 ± 0.02	0.0 ± 0.1	...	Y	E
	E	10	4.4	−111	0.03 ± 0.02	0.1 ± 0.1	...	Y	E
1413+135[a]	B[b]	6	2.1	−113	0.25 ± 0.08	3.9 ± 1.2	1989.8 ± 2.7	Y	E
	C	4	3.8	−111	0.37 ± 0.15	5.8 ± 2.4	...	Y	P
	F	3	6.6	−109	0.45 ± 0.15	7.1 ± 2.4	1984.9 ± 4.9	Y	F
1508−055	B[b]	7	1.7	85	0.10 ± 0.02	6.2 ± 1.2	1981.9 ± 3.2	Y	E
	C	5	4.9	83	0.53 ± 0.30	31.4 ± 18.1	...	Y	P
1510−089[a]	B[b]	5	2.8	−26	0.85 ± 0.05	18.9 ± 1.0	1994.6 ± 0.2	Y	E
	C	3	2.3	−32	0.57 ± 0.03	12.8 ± 0.7	1995.0 ± 0.2	N	F
1532+016	B[b]	6	1.1	130	0.21 ± 0.01	13.7 ± 0.9	1992.6 ± 0.4	Y	E
	D	6	6.6	143	0.06 ± 0.03	4.1 ± 1.9	...	N	G
1546+027[a]	B[b]	3	1.2	175	0.05 ± 0.03	1.3 ± 0.8	...	N	F
1548+056[a]	B[b]	5	4.4	10	0.052 ± 0.004	3.5 ± 0.3	1912.6 ± 7.0	Y	E

TABLE 2—*Continued*

Object (1)	Component (2)	N (3)	$\langle R \rangle$ (mas) (4)	$\langle \vartheta \rangle$ (deg) (5)	μ_r (mas yr^{-1}) (6)	$\beta_{\rm app}$ (7)	t_0 (yr) (8)	Distinct Component (9)	Rating (10)
1606+106[a]	B[b]	5	0.9	−58	0.30 ± 0.02	18.4 ± 1.4	1994.8 ± 0.3	N	G
	C	4	1.2	−53	0.38 ± 0.03	23.2 ± 2.1	1994.0 ± 0.3	N	G
	D	3	1.5	−52	0.36 ± 0.02	21.6 ± 1.3	1991.9 ± 0.2	N	F
	E	3	2.1	−40	0.50 ± 0.03	30.1 ± 1.6	1991.9 ± 0.2	N	F
	F	3	0.6	−61	0.196 ± 0.001	11.8 ± 0.1	1996.16 ± 0.00	N	F
1611+343[a]	B[b]	5	2.9	173	0.06 ± 0.04	4.2 ± 2.6	...	Y	E
1633+382[a]	B[b]	8	1.5	−86	0.15 ± 0.03	11.5 ± 2.0	1987.5 ± 1.8	Y	E
	C	7	2.6	−82	0.10 ± 0.03	7.3 ± 2.6	...	N	G
1641+399[a]	B[b]	9	1.7	−95	0.49 ± 0.03	17.0 ± 0.9	1993.9 ± 0.2	Y	E
	C	5	0.9	−101	0.37 ± 0.03	12.8 ± 1.0	1995.4 ± 0.2	Y	E
1642+690	B[b]	5	2.2	−162	0.38 ± 0.04	16.0 ± 1.8	1991.9 ± 0.7	Y	E
	D	4	9.9	−166	−0.04 ± 0.05	−1.6 ± 2.3	...	Y	E
1652+398	B	5	2.7	142	0.06 ± 0.26	0.1 ± 0.6	...	Y	P
	C[b]	6	7.5	109	0.09 ± 0.05	0.2 ± 0.1	...	Y	E
1655+077[a]	B	5	3.7	−38	0.43 ± 0.03	15.3 ± 1.0	1988.9 ± 0.6	Y	E
	C[b]	5	8.0	−44	0.07 ± 0.03	2.4 ± 0.9	...	Y	E
1656+053	B[b]	4	0.7	72	0.09 ± 0.02	4.4 ± 0.8	1990.0 ± 1.4	N	G
1656+477	B[b]	5	1.1	0	0.04 ± 0.04	2.8 ± 3.0	...	N	G
	C	5	7.0	−19	0.06 ± 0.06	4.5 ± 4.6	...	Y	E
1730−130[a]	B[b]	4	5.0	17	0.48 ± 0.12	23.3 ± 5.6	1987.5 ± 2.5	Y	G
1749+096[a]	B	4	4.6	29	0.06 ± 0.07	1.2 ± 1.3	...	Y	E
	C[b]	4	0.7	34	0.15 ± 0.03	3.1 ± 0.5	1993.5 ± 0.8	N	G
1749+701	B[b]	6	2.3	−66	0.01 ± 0.03	0.4 ± 1.1	...	Y	E
	C	3	3.2	−58	−0.084 ± 0.003	−3.6 ± 0.1	...	N	F
	D	3	1.3	−76	0.08 ± 0.06	3.4 ± 2.6	...	N	F
1758+388[a]	B[b]	4	0.4	−98	0.002 ± 0.013	0.2 ± 1.1	...	N	G
1800+440[a]	B[b]	5	2.6	−163	0.49 ± 0.05	18.5 ± 2.0	1992.5 ± 0.6	Y	E
	C	4	4.4	−155	0.56 ± 0.14	21.2 ± 5.3	1989.1 ± 2.0	Y	G
1803+784[a]	B[b]	6	1.4	−94	−0.01 ± 0.01	−0.5 ± 0.4	...	Y	E
1807+698	B[b]	7	2.5	−96	0.01 ± 0.04	0.0 ± 0.1	...	Y	E
	C	8	5.2	−94	0.12 ± 0.04	0.4 ± 0.1	...	Y	E
	D	3	6.8	−97	0.85 ± 0.47	2.9 ± 1.6	...	Y	P
	E	4	0.6	−97	0.26 ± 0.08	0.9 ± 0.3	1996.9 ± 0.8	N	F
1823+568[a]	B[b]	7	1.7	−158	−0.003 ± 0.040	−0.1 ± 1.5	...	Y	E
	C	7	6.7	−161	0.09 ± 0.03	3.4 ± 1.1	1923.0 ± 23.4	Y	E
1828+487[a]	B	3	1.2	−20	0.23 ± 0.03	9.2 ± 1.3	1993.5 ± 0.7	N	F
	C	3	3.5	−23	0.38 ± 0.15	14.8 ± 5.8	...	Y	F
	D[b]	3	9.6	−32	0.26 ± 0.01	10.1 ± 0.4	1961.5 ± 1.6	Y	G
1845+797	B	9	5.5	−41	0.54 ± 0.03	2.1 ± 0.1	1987.2 ± 0.6	Y	E
	C[b]	10	7.2	−36	0.60 ± 0.01	2.3 ± 0.1	1985.7 ± 0.3	Y	E
1901+319	B[b]	7	0.8	122	0.03 ± 0.02	0.9 ± 0.7	...	N	G
	C	7	15.8	120	0.00 ± 0.01	0.0 ± 0.5	...	Y	E
1921−293	B	4	5.7	24	0.19 ± 0.06	4.2 ± 1.3	1968.9 ± 8.9	Y	E
	C	4	2.3	−1	0.17 ± 0.06	3.7 ± 1.2	1984.7 ± 4.5	N	G
	D[b]	4	0.5	−29	0.01 ± 0.01	0.2 ± 0.2	...	N	G
1928+738[a]	B[b]	8	2.1	165	0.29 ± 0.03	5.6 ± 0.6	1990.3 ± 0.7	Y	E
	C	6	3.6	161	0.30 ± 0.08	5.8 ± 1.5	1984.7 ± 3.1	Y	E
	E	5	0.8	156	0.12 ± 0.06	2.3 ± 1.1	...	Y	E
1957+405[a]	B	5	6.0	−78	0.12 ± 0.02	0.5 ± 0.1	1950.6 ± 8.0	N	G
	D	8	3.0	−79	0.18 ± 0.02	0.7 ± 0.1	1981.4 ± 1.6	N	G
	E	8	2.2	−80	0.19 ± 0.03	0.7 ± 0.1	1986.0 ± 1.6	N	G
	F	6	1.7	−79	0.22 ± 0.03	0.8 ± 0.1	1990.3 ± 1.1	N	G
	G[b]	8	1.2	−79	0.16 ± 0.03	0.6 ± 0.1	1990.0 ± 1.6	N	G
	I	7	0.8	−79	0.10 ± 0.02	0.4 ± 0.1	1990.6 ± 1.6	N	G
	J	5	0.5	−123	0.05 ± 0.02	0.2 ± 0.1	1989.6 ± 3.1	N	G
	K	7	6.6	109	0.00 ± 0.14	0.0 ± 0.5	...	Y	G
	L	8	3.0	115	0.05 ± 0.03	0.2 ± 0.1	...	Y	E
2005+403[a]	B[b]	5	3.2	120	0.16 ± 0.04	12.3 ± 3.0	1978.2 ± 4.8	Y	E
2007+776	B[b]	8	1.4	−92	0.00 ± 0.03	0.0 ± 0.6	...	Y	E
	D	6	6.8	−91	−0.04 ± 0.23	−0.8 ± 4.9	...	Y	P
2021+317[a]	B[b]	5	3.4	166	0.14 ± 0.05	...	...	Y	E
	C	3	1.0	−172	0.02 ± 0.02	...	...	N	F
2021+614[a]	B	6	3.9	34	0.04 ± 0.04	0.6 ± 0.5	...	Y	E
	C[b]	6	3.1	−149	0.05 ± 0.04	0.8 ± 0.6	...	Y	E

TABLE 2—*Continued*

Object (1)	Component (2)	N (3)	$\langle R \rangle$ (mas) (4)	$\langle \vartheta \rangle$ (deg) (5)	μ_r (mas yr^{-1}) (6)	$\beta_{\rm app}$ (7)	t_0 (yr) (8)	Distinct Component (9)	Rating (10)
2113+293	B[b]	5	0.3	177	0.02 ± 0.01	1.4 ± 0.3	1985.1 ± 3.2	N	G
2128−123[a]	B[b]	3	3.7	−143	-0.07 ± 0.01	-2.0 ± 0.2	...	Y	G
2131−021[a]	C[b]	4	0.8	105	0.12 ± 0.03	7.7 ± 1.6	1991.9 ± 1.4	N	G
2134+004[a]	B[b]	6	1.9	−99	0.02 ± 0.02	1.5 ± 1.7	...	Y	E
2136+141[a]	B[b]	6	0.3	−72	0.02 ± 0.01	1.8 ± 1.4	...	N	G
2144+092	B[b]	3	0.6	83	0.03 ± 0.04	1.5 ± 2.0	...	N	F
2145+067[a]	B	8	0.3	−95	-0.01 ± 0.01	-0.6 ± 0.4	...	N	G
	C[b]	8	0.6	−119	0.027 ± 0.003	1.4 ± 0.2	1974.2 ± 2.3	N	G
	D	8	1.0	−118	0.03 ± 0.01	1.4 ± 0.4	1960.4 ± 9.6	N	G
2200+420[a]	B[b]	7	2.4	−172	1.41 ± 0.13	6.5 ± 0.6	1995.1 ± 0.2	Y	E
	C	5	2.5	−171	1.12 ± 0.22	5.2 ± 1.0	1995.6 ± 0.5	Y	E
	D	4	2.7	−172	0.99 ± 0.18	4.5 ± 0.8	1996.7 ± 0.5	Y	E
	E	3	1.9	−161	1.09 ± 0.37	5.0 ± 1.7	...	Y	P
2201+315[a]	B[b]	6	2.8	−145	0.34 ± 0.02	6.3 ± 0.5	1989.7 ± 0.6	Y	E
2209+236[a]	B[b]	4	1.5	18	0.04 ± 0.04	2.3 ± 2.4	...	N	G
2223−052[a]	B[b]	6	1.9	102	0.49 ± 0.09	32.5 ± 6.0	1994.0 ± 0.8	Y	E
	C	7	5.2	98	0.31 ± 0.03	20.4 ± 1.9	1981.4 ± 1.6	Y	E
2230+114[a]	B[b]	8	1.9	143	0.03 ± 0.04	1.4 ± 2.1	...	Y	E
	C	6	4.6	166	-0.05 ± 0.03	-2.7 ± 1.6	...	Y	E
	D	5	6.5	156	0.00 ± 0.01	0.0 ± 0.8	...	Y	E
	E	3	17.8	141	-0.23 ± 0.37	-12.3 ± 19.9	...	N	P
2234+282	B[b]	5	1.2	−97	0.12 ± 0.05	5.1 ± 2.2	...	Y	E
2243−123[a]	B[b]	4	2.7	15	0.29 ± 0.03	10.7 ± 1.1	1988.7 ± 0.9	Y	E
	C	3	10.3	25	-0.14 ± 0.05	-4.9 ± 1.9	...	Y	G
	D	4	11.3	33	0.11 ± 0.10	4.1 ± 3.5	...	Y	G
2251+158[a]	B[b]	8	5.2	−86	0.04 ± 0.04	1.9 ± 2.1	...	Y	E
2345−167[a]	B[b]	5	1.7	124	0.03 ± 0.05	1.0 ± 1.6	...	Y	E

NOTES.—Col. (1): IAU name. Col. (2): Component identifier. Col. (3): Number of epochs with measured position. Col. (4): Mean radial position, relative to the core. Col. (5): Mean structural position angle, relative to the core. Col. (6): Angular radial speed and 1 σ uncertainty. Col. (7): Radial speed in units of the speed of light and 1 σ uncertainty, computed assuming $H_0 = 70$ km s^{-1} Mpc^{-1}, $\Omega_m = 0.3$, and $\Omega_\Lambda = 0.7$. Col. (8): Extrapolated epoch of origin and uncertainty. Col. (9): Does the component satisfy the second criterion in § 3, i.e., is it a well-defined feature? Col. (10): Overall quality rating. Table 2 is also available in machine-readable form in the electronic edition of the *Astrophysical Journal*.

[a] Source is a member of the representative sample.

[b] Component is the brightest.

[c] Motions for 0316+413 that are taken from unpublished data do not appear in Fig. 1. The motions for 0238−084 are from Vermeulen et al. (2003b).

simplest model, which has only one value of γ that is the same in all sources and also has $\beta_b = \beta_p$ in all sources, is not tenable. They showed that either there must be a distribution of γ among the sources, or $\beta_b \neq \beta_p$. Most likely, there is both some distribution of γ and also a difference between γ_p and γ_b.

The apparent transverse velocity of an approaching component with a pattern Lorentz factor γ_p reaches a maximum apparent speed $\beta_p\gamma_p$ when the component moves at an angle $\sin\theta = 1/\gamma_p$ to the line of sight. For the corresponding component in the receding jet, the observed velocity is $\beta_p/2$.

3. A change in the apparent flux density, S, of a moving component over its stationary value, S_0, by a factor

$$S/S_0 = \delta^{x-\alpha}, \tag{3}$$

where α is the spectral index and x has a value of 2 for a continuous jet or 3 for discrete components (see, e.g., Urry & Padovani 1995).

The Doppler factor is sharply peaked along the direction of motion, so sources with highly relativistic jets that happen to be pointed close to the line of sight will appear strongly boosted and hence are likely to be selected in a flux-limited sample. Although the jets may be intrinsically two-sided, unless they are very close to the plane of the sky, they will appear highly asymmetric (i.e., one-sided) since the radiation from the receding jet is highly beamed away from the observer.

Equation (3) has the important consequence that the strongest, most compact radio sources we observe tend to have highly relativistic jets that are aligned close to the line of sight, and they will therefore likely display superluminal motion. The most probable angle for sources selected on the basis of beamed flux density alone is close to $(2\gamma)^{-1}$, where $\beta_{\rm app} \sim \gamma/2$ (Vermeulen & Cohen 1994). The distribution of observed speeds and flux densities is dependent on the distributions of γ, redshift, and the intrinsic luminosity function.

This is illustrated in Figure 3, where we show the predicted distribution of apparent velocities for three different models. If the effect of Doppler boosting is ignored, for example, if the observed motions are due to the propagation of shocks rather than actual bulk motion, then most jets will lie close to the plane of the sky and have apparent speeds $\beta_{\rm app}$ close to β_p. If we take into account the effect of Doppler boosting, then, in a flux-limited sample, with a single Lorentz factor, most sources are found to lie close to the line of sight and have an apparent velocity $\beta_{\rm app} \sim \beta_p\gamma$. In the typical situation that we consider, where $\beta_p \sim 1$, in the absence of Doppler boosting most sources appear to have an apparent velocity close to c,

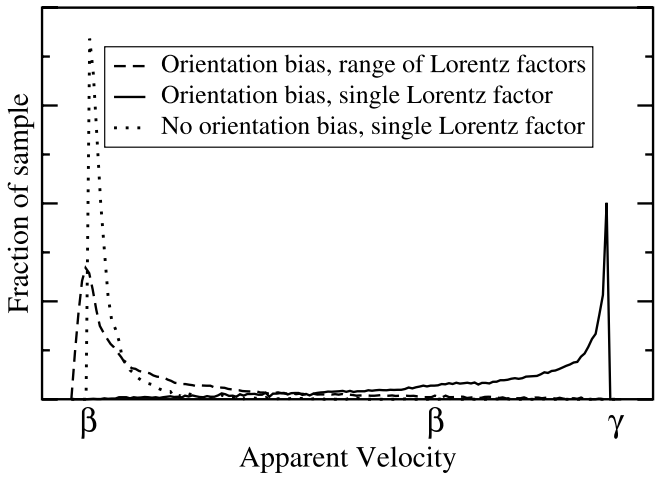

FIG. 3.—Predicted distributions of β_{app} when the sample has randomly oriented jets all with the same Lorentz factor γ (*dotted line*), when the sample has sources drawn from such a jet population but based on flux density that can be enhanced by Doppler boosting (*solid line*), and for a Doppler boosting with a range of Lorentz factors that favors low values of the Lorentz factor (*dashed line*).

whereas in the Doppler boosted case most sources have an apparent velocity close to γc. Note that in the absence of Doppler boosting there are virtually no sources with apparent speeds less than βc since this would require rare end-on orientations. The randomly oriented model also drops much more sharply with increasing β than the model with a range of Lorentz factors.

Blandford & Königl (1979) suggested that one of the observed jet components might be the stationary feature of the approaching jet at the point where it becomes optically thin, so that the flux density of this "core" component, as well as the moving component, is Doppler boosted. The observed overall spectrum is typically flat, which may be due to the superposition of different parts of the jet, which each have different Doppler factors, causing the synchrotron cutoff to appear at different frequencies. Consideration of differential Doppler boosting led to the concept of unified models (e.g., Orr & Browne 1982; Barthel 1989; Urry & Padovani 1995), which is usually invoked to understand the observed differences in the properties of quasars, active galaxies, and BL Lac objects as due to the orientation of the relativistic beam and an obscuring torus with respect to the line of sight. Thus, comparison of apparent jet speeds with optical classification is an effective test of these unified models and also serves to refine their parameters.

4.2. *Jet Kinematics*

The motion statistics collected for our sample address many physical questions related to relativistic jets. The process of their formation, that is, the initial acceleration and collimation of the flow, can be constrained by studying the speeds as a function of distance from the beginning of the visible jet (often referred to as the "core") and also by comparing the times when flares occur with the back-extrapolated epochs at which moving features appear to originate. Long-term multiepoch observations can show whether there are accelerations or decelerations farther down the jets and whether radio features follow straight or curved trajectories.

In order to discriminate between various jet models and then to refine the relevant ones, it is important to establish whether jets exist as predefined channels, along which multiple moving features can be seen, or whether instead successive components follow different trajectories, at either the same or at different speeds. Viable models of jet formation will also need to be able to reproduce the observed Lorentz factor distribution. The moving features may in fact be patterns, caused by the propagation of shocks rather than the flow of matter. This can be studied by comparing the Lorentz factors inferred from the motions to the Lorentz factors estimated by other means, such as variability, brightness temperature, and (possibly) the presence of X-ray and gamma-ray emission. By probing for correlations between the apparent velocities and other quantities such as the radio or X-ray luminosity, more can be learned about the physical parameters relevant for jet formation. Finally, studying the distribution of velocities as a function of optical host type is relevant to constraining unification models.

Most of the jets in our study are well collimated and are unresolved transverse to their flow, although there often is significant curvature. In some radio galaxies with two-sided structure, the appearance of the source is very frequency dependent, suggesting free-free absorption in a disk or torus, probably associated with the accretion disk surrounding the central engine.

We found several jet features to have apparent negative velocities; that is, they appear to be approaching rather than receding from the core. Most of these apparently negative velocities are consistent, within the errors, with no significant motion. Observations extending over a longer time frame are needed to determine if these inward motions are real. Apparent inward motion may be produced if there is a newly emerging jet feature that is ejected from the core and the combination is not resolved by our beam. This would cause a shift in the measured position of the centroid and a corresponding decrease with time in the apparent separation of the core and other jet features. It is also possible that the true core is not seen, possibly as a result of absorption, and that the only observed features are parts of a jet that are moving with different velocities. If the farthest component is moving with a slower velocity than the one closest to the obscured core, then they will appear to be approaching each other. The apparent decrease in component separation from the core could also be due to component motion away from the core along a highly curved jet that bends back toward the line of sight, so that the projected separation from the core appears to decrease with time. Finally, the moving features could be only patterns in the flow, some of which might even be moving backward. Istomin & Pariev (1996) have discussed an electron-positron jet model where an observer located close to the direction of motion will see backward-moving knots. We note that any model involving patterns must account for the very large numbers of observed outward motions, as opposed to inward ones. For this reason, many of the simplest "moving marquee" models for superluminal motion have already been ruled out. In the case of 0735+178, the most distant feature appears to be moving inward, but this is probably an artifact of the complex brightness distribution whose centroid shifts when the intensity distribution changes.

4.2.1. *Velocity Distributions*

Figure 4 shows the distribution of the observed values of $\beta_{app} = 1.58 \times 10^{-2} \mu D_A (1 + z)$, where D_A is the angular size distance to the radio source in megaparsecs and the angular velocity, μ, is in mas yr^{-1}. Figure 5 shows the same distributions for those jets found in the representative subsample

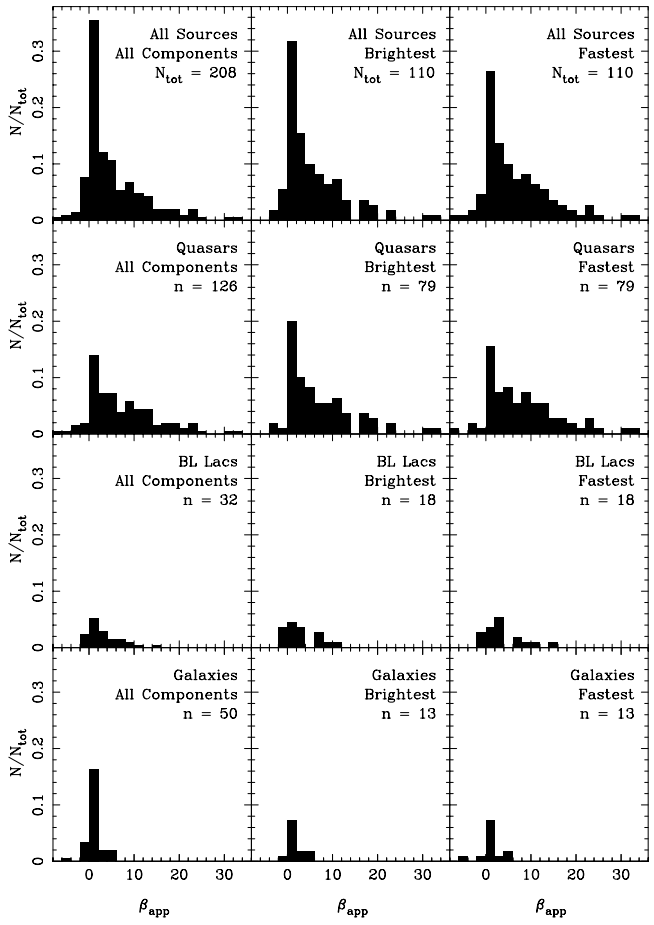

FIG. 4.—Distribution of the apparent linear velocity in all sources with a quality code E or G and that have measured redshifts. The left panels display the distribution for all individual features that we have observed. Distributions in the middle and right panels show only one feature per source, the brightest or the fastest, respectively. Sources are divided by optical class in the second, third, and fourth rows of the figure.

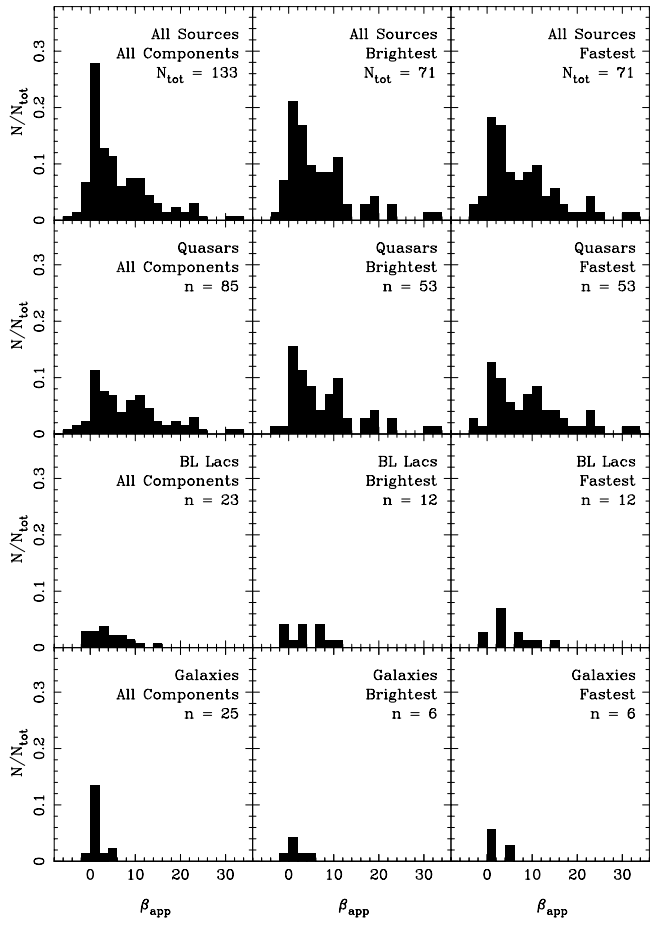

FIG. 5.—Same distributions as in Fig. 4, except that only those sources contained in our representative flux density–limited subsample are included.

described in § 2.2. We include in these figures only those jet features that we have been able to measure with a quality code of E or G and that have measured redshifts.

The middle and right panels of Figures 4 and 5 show the motions of only one feature per source, the brightest and the fastest, respectively. The brightest feature in each jet is defined as the one with the largest peak flux density at the epoch for which the source image was presented in Papers I and II, although in nearly all cases this does not change over the period covered by these observations. These features generally have well-determined motions; however, in a few cases, the brightest jet feature does not have an E or G quality code, usually because it has a large diffuse structure. In these cases, we have substituted the brightest component that did have an E or G quality code. For the right panels of Figure 4, the fastest feature within a source is simply defined as the one with the largest (absolute) linear speed with a quality code of either E or G.

K-S tests indicate that at a 95% confidence level there is no difference in the distribution of the jet speeds, independent of whether we consider the brightest, fastest, or even all the jet features within a source. We consider the brightest feature of each source to be the most representative for our analysis, since in the case of sources with weak secondary features observations having a limited sensitivity or dynamic range might only detect the brightest jet feature.

The distributions shown in Figures 4 and 5 are also subdivided according to optical class. We find that the velocity distributions for the quasars, radio galaxies, and BL Lac objects are mostly concentrated in the same range ($0 < \beta_{\rm app} < 15$). However, the quasars have a tail ranging up to $\beta_{\rm app} \sim 34$, while jets associated with active galaxies have a narrow range of velocities with $\beta_{\rm app} \leq 6$. A K-S test confirms at the 98% confidence level that the quasars have a different speed distribution than the galaxies and BL Lac objects, while the distributions of speeds for the galaxies and BL Lac objects are statistically indistinguishable. Examination of Figures 4 and 5 suggests that the distribution of quasar velocities may be bimodal with a minimum near $\beta_{\rm app} \sim 5$. We have compared our observed distributions with one and two Gaussian distributions and find in each case a significantly lower value of reduced χ^2 for the two-component distribution for all of the quasar distributions. However, we are reluctant to quantify this further, as the observed distributions are clearly more complex than can be represented by two Gaussians.

We have also compared the dispersion in the speed of different features within each jet with the dispersion of the average jet speeds. We find that the dispersion of the average jet speeds among the 50 sources with two or more features with quality factors E or G is $6.3c$, whereas in all but four jets

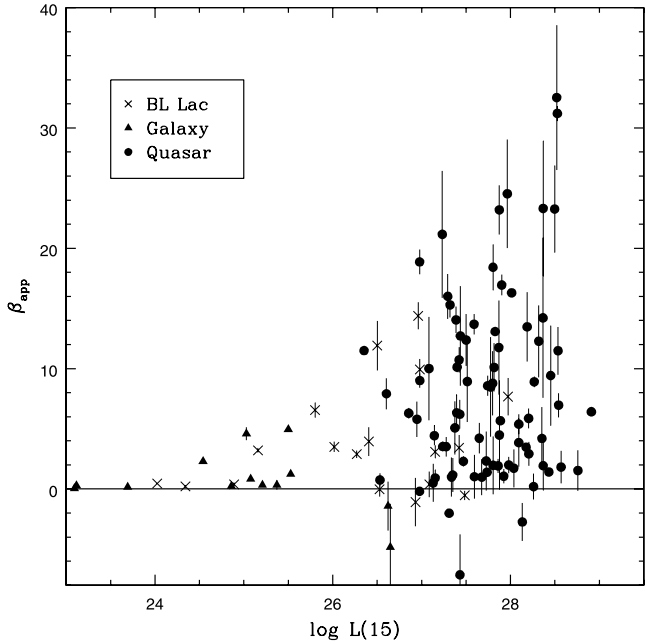

FIG. 6.—Apparent speed of the fastest feature found in 110 jets as a function of the radio luminosity.

(92%) the dispersion in the speed of individual jet features is smaller than this value. This suggests that there is an underlying flow, characteristic of each jet, that determines the speed of individual features with the jet.

4.2.2. *Apparent Speed and Apparent Luminosity*

Figure 6 shows the relation between β_{app} and apparent VLBA core luminosity at 15 GHz. There is a distinct upper envelope to the distribution, which is very similar to that found at 5 GHz in the Caltech-Jodrell flat-spectrum survey by Vermeulen (1995). In particular, the low-luminosity sources all have slow apparent speeds. If we divide the sources at the median luminosity of $L_{15} < 10^{27.4}$ W Hz^{-1}, a K-S test yields less than a 1% probability that speed distributions for the brightest components of the high- and low-luminosity sources have the same parent distribution. We note that if the apparent jet speeds that we are measuring are simply random patterns, then no envelope would be expected in Figure 6.

As discussed by Lister & Marscher (1997), the presence of this envelope does not necessarily imply that *intrinsically* faint jets have low *intrinsic* speeds. As discussed in § 4.3.1, in practice there is likely to be a spread in Lorentz factors. The lowest luminosity sources in a flux-limited sample will tend to lie at low redshifts, where the comoving volume element is small. Ignoring evolutionary effects and assuming a constant comoving space density and a steep luminosity function, these sources will therefore be representative of the most common jets in the parent population. The probability of any of them having *both* a high Lorentz factor and a small viewing angle will be very small, especially if the parent population is dominated by low Lorentz factor jets [i.e., $n(\gamma) \propto \gamma^{-1.5}$ as found by Lister & Marscher 1997]. This may therefore explain why none of the low-luminosity sources in Figure 6 are highly superluminal.

4.2.3. *Nonradial and Bent Trajectories*

For most of the sources in our sample we have determined only the radial speed and position angle of the motion with respect to the assumed core component. For those sources with sufficiently high quality data, we also computed the full two-dimensional vector proper motion on the sky. This was accomplished by fitting separately for the proper motion in both right ascension and declination. These results were combined to form a vector velocity, determined by the speed, μ, and the direction, ϕ, on the sky relative to the radio core. We are particularly interested in comparing the direction of motion, ϕ, to the mean structural position angle of the jet, $\langle\vartheta\rangle$.

Table 3 compiles the vector proper motions for all jet components in our sample that have at least five epochs of observation and for which the vector velocity is of at least 5 σ significance. These criteria guarantee that only the highest quality vector motions are used in our comparison of velocity direction to structural position angle. Of the 60 component motions that meet these criteria, we find that 20 are significantly "nonradial," meaning that the velocity direction, ϕ, differs by at least 3 σ from the mean structural position angle, $\langle\vartheta\rangle$. These nonradial motions are highlighted in bold in Table 3.

Nonradial motions do not follow a direction that extrapolates back to the jet origin and are by definition considered nonballistic. The occurrence of such nonballistic motions in approximately one-third of the highest quality motions we examined is striking. Assuming that the observed velocities trace the underlying jet flow, this result indicates that bends in jet direction and/or jet collimation are common. The actual bends may be small, only a few degrees, but the observed bends can be large, of the order of 90°, since they appear amplified by projection.

In Figure 7 we show tracks in the right ascension–declination plane of several sources that have clearly defined nonradial or bent trajectories. In general, the trajectories are bent toward the next structure down the jet, whether seen directly in our maps or in published larger scale images. This suggests that jet features may trace out a flow in a preexisting curved channel. Sources 1226+023 (3C 273), 1219+285, 1532+016, and 2200+420 (BL Lac) are excellent examples of this trend. In 1548+056, the component motion appears to be transverse to the main jet direction that is known from lower resolution images, and is hinted at in our images, to lie to the north. However, the motion we observe is directed toward the small extension toward the east, and looking back toward the core, the jet ridgeline appears to curve into the component from the opposite direction.

In 3C 390.3 (1845+797) the two most prominent features appear to be moving with a similar speed of about 2.5c but along slightly different trajectories of 27° and 30°. Neither trajectory is aligned with the direction of the core or with the narrow 60″ jet that points toward one of the distant hot spots in position angle 35° (Alef et al. 1996). This is a clear exception to the trend identified above.

In general we do not have sufficient data to robustly detect changes in velocity, although the high incidence of nonballistic motion implies that such changes must occur. However, in BL Lac, there is evidence that the moving feature traces the curved ridgeline of the jet. Moreover, we have previously reported an abrupt change in both speed and direction in 3C 279 that occurred in 1998 (Homan et al. 2003).

4.2.4. *Two-sided Sources*

Seven sources in Table 2 display two-sided structure in which the jet flow appears bidirectional away from a central core. We have previously reported our results on the two-sided source NGC 1052 (Vermeulen et al. 2003b), where the component motion is close to the plane of the sky and multiple

TABLE 3

VECTOR PROPER-MOTION RESULTS

Object (1)	Component (2)	N (3)	$\langle R \rangle$ (mas) (4)	$\langle \vartheta \rangle$ (deg) (5)	μ (mas yr^{-1}) (6)	ϕ (deg) (7)	$\beta_{\rm app}$ (8)	$\lvert\langle \vartheta \rangle - \phi\rvert$ (deg) (9)
0035+413	B	5	1.5 ± 0.0	103.7 ± 0.8	0.10 ± 0.02	121.8 ± 8.2	6.6 ± 1.2	18.1 ± 8.2
0055+300	B	5	0.9 ± 0.0	−54.2 ± 1.6	0.14 ± 0.02	−52.3 ± 7.3	0.2 ± 0.0	1.9 ± 7.5
0106+013	C	5	2.1 ± 0.0	−112.7 ± 1.2	0.27 ± 0.03	−119.6 ± 7.4	22.4 ± 2.1	6.9 ± 7.5
0149+218	C	6	5.0 ± 0.1	−21.9 ± 1.1	0.29 ± 0.04	−26.3 ± 9.9	18.7 ± 2.3	4.5 ± 9.9
0234+285	**B**	**6**	**3.5 ± 0.1**	**−12.6 ± 0.6**	**0.25 ± 0.05**	**11.6 ± 4.2**	**14.7 ± 2.8**	**24.2 ± 4.3**
0333+321	B	9	2.7 ± 0.0	123.3 ± 0.2	0.18 ± 0.01	120.3 ± 1.8	11.0 ± 0.4	3.0 ± 1.8
	C	9	4.9 ± 0.0	126.0 ± 0.5	0.20 ± 0.02	135.0 ± 6.8	12.2 ± 1.4	9.0 ± 6.8
0336−019	B	5	1.4 ± 0.1	66.9 ± 1.8	0.22 ± 0.04	67.1 ± 7.0	10.1 ± 1.7	0.2 ± 7.2
0415+379	D	6	3.3 ± 0.1	65.9 ± 0.8	1.52 ± 0.04	65.3 ± 1.4	4.9 ± 0.1	0.6 ± 1.6
0430+052	B	10	4.7 ± 0.1	−110.8 ± 0.6	1.77 ± 0.06	−108.7 ± 1.1	3.9 ± 0.1	2.1 ± 1.3
	C	8	6.1 ± 0.2	−105.9 ± 1.1	1.81 ± 0.17	−100.0 ± 3.7	4.0 ± 0.4	5.9 ± 3.8
	G	9	3.0 ± 0.1	−112.0 ± 1.9	1.59 ± 0.10	−105.9 ± 2.5	3.5 ± 0.2	6.1 ± 3.2
	H	5	2.6 ± 0.2	−118.4 ± 2.6	2.08 ± 0.20	−114.8 ± 3.5	4.6 ± 0.4	3.6 ± 4.4
0735+178	**D**	**5**	**4.0 ± 0.1**	**63.9 ± 0.9**	**0.18 ± 0.03**	**−119.1 ± 12.6**	...	**177.0 ± 12.7**
0736+017	**B**	**6**	**4.2 ± 0.1**	**−70.0 ± 1.6**	**0.96 ± 0.04**	**−87.3 ± 4.3**	**11.9 ± 0.5**	**17.4 ± 4.6**
	D	5	10.0 ± 0.1	−87.8 ± 0.2	0.39 ± 0.06	−86.1 ± 3.1	4.8 ± 0.8	1.7 ± 3.1
	E	5	2.1 ± 0.1	−67.8 ± 2.2	0.86 ± 0.09	−72.0 ± 3.8	10.6 ± 1.1	4.2 ± 4.4
0738+313	B	8	2.8 ± 0.0	179.4 ± 0.3	0.07 ± 0.01	157.7 ± 7.6	2.5 ± 0.4	21.6 ± 7.6
0745+241	C	8	3.1 ± 0.1	−63.1 ± 1.0	0.33 ± 0.04	−50.0 ± 6.5	8.2 ± 1.0	13.1 ± 6.5
0748+126	B	6	1.7 ± 0.0	120.1 ± 0.4	0.12 ± 0.01	129.3 ± 4.5	5.9 ± 0.5	9.3 ± 4.5
0754+100	**B**	**5**	**4.0 ± 0.1**	**14.6 ± 0.9**	**0.76 ± 0.13**	**−7.1 ± 4.5**	**12.9 ± 2.1**	**21.7 ± 4.6**
0814+425	B	6	0.9 ± 0.0	89.6 ± 0.8	0.18 ± 0.02	86.5 ± 2.0	2.9 ± 0.3	3.1 ± 2.1
0823+033	C	6	2.4 ± 0.1	14.1 ± 0.6	0.48 ± 0.04	10.8 ± 1.6	14.5 ± 1.1	3.3 ± 1.7
	D	6	1.1 ± 0.1	31.9 ± 3.0	0.31 ± 0.05	31.3 ± 6.4	9.4 ± 1.5	0.6 ± 7.1
0851+202	C	5	1.0 ± 0.0	−91.9 ± 1.0	0.52 ± 0.04	−90.6 ± 2.5	9.9 ± 0.9	1.2 ± 2.7
	D	5	0.9 ± 0.1	−102.4 ± 1.5	0.38 ± 0.06	−111.4 ± 5.0	7.2 ± 1.1	9.0 ± 5.3
0917+449	B	6	1.2 ± 0.0	177.7 ± 0.5	0.07 ± 0.01	−176.1 ± 5.7	5.9 ± 0.8	6.2 ± 5.7
0953+254	**C**	**5**	**1.0 ± 0.0**	**−129.3 ± 1.4**	**0.10 ± 0.00**	**−96.6 ± 9.5**	**4.2 ± 0.1**	**32.7 ± 9.6**
1012+232	B	5	2.2 ± 0.0	109.7 ± 0.4	0.27 ± 0.02	111.7 ± 1.8	9.0 ± 0.6	2.0 ± 1.8
1015+359	**B**	**6**	**1.3 ± 0.1**	**−172.3 ± 0.4**	**0.21 ± 0.04**	**177.2 ± 0.6**	**12.6 ± 2.2**	**10.4 ± 0.7**
1101+384	**C**	**7**	**1.4 ± 0.0**	**−38.8 ± 1.3**	**0.23 ± 0.02**	**−57.1 ± 3.8**	**0.5 ± 0.0**	**18.3 ± 4.0**
	D	6	0.8 ± 0.0	−30.3 ± 2.8	0.17 ± 0.02	−26.8 ± 9.2	0.4 ± 0.0	3.5 ± 9.7
1127−145	**C**	**7**	**4.1 ± 0.0**	**83.0 ± 0.1**	**0.09 ± 0.01**	**70.4 ± 3.1**	**5.5 ± 0.8**	**12.6 ± 3.1**
1219+285	**D**	**7**	**11.0 ± 0.1**	**106.8 ± 0.3**	**0.59 ± 0.03**	**143.6 ± 3.0**	**4.0 ± 0.2**	**36.7 ± 3.0**
1226+023	**B**	**11**	**6.1 ± 0.1**	**−112.7 ± 0.4**	**1.05 ± 0.04**	**−119.6 ± 1.6**	**10.9 ± 0.4**	**6.9 ± 1.7**
	C	7	9.6 ± 0.1	−120.2 ± 0.7	1.36 ± 0.08	−119.1 ± 2.9	14.1 ± 0.9	1.1 ± 3.0
	D	8	10.8 ± 0.2	−119.5 ± 1.0	0.83 ± 0.16	−119.7 ± 10.3	8.6 ± 1.7	0.2 ± 10.3
	E	10	3.3 ± 0.1	−116.1 ± 1.1	1.27 ± 0.07	−115.4 ± 2.3	13.1 ± 0.8	0.7 ± 2.5
	F	6	18.7 ± 0.2	−123.1 ± 0.6	0.83 ± 0.14	−140.5 ± 10.6	8.5 ± 1.5	17.4 ± 10.6
1253−055	**B**	**10**	**3.3 ± 0.0**	**−115.9 ± 0.5**	**0.29 ± 0.01**	**−130.3 ± 3.1**	**9.1 ± 0.4**	**14.4 ± 3.1**
1345+125	C	5	2.0 ± 0.0	164.2 ± 0.8	0.16 ± 0.01	173.3 ± 7.3	1.2 ± 0.1	9.1 ± 7.3
	E	**5**	**9.8 ± 0.0**	**161.8 ± 0.1**	**0.04 ± 0.01**	**114.3 ± 15.1**	**0.3 ± 0.1**	**47.5 ± 15.1**
1510−089	B	5	2.8 ± 0.1	−26.5 ± 0.9	0.85 ± 0.04	−23.2 ± 2.1	19.0 ± 0.8	3.3 ± 2.3
1532+016	**B**	**6**	**1.1 ± 0.0**	**130.4 ± 1.0**	**0.21 ± 0.01**	**146.8 ± 2.5**	**14.3 ± 0.7**	**16.4 ± 2.7**
1548+056	**B**	**5**	**4.4 ± 0.0**	**10.4 ± 0.3**	**0.12 ± 0.01**	**74.4 ± 2.9**	**7.7 ± 0.8**	**64.1 ± 2.9**
1606+106	B	5	0.9 ± 0.0	−58.0 ± 2.5	0.31 ± 0.02	−47.8 ± 4.0	18.7 ± 1.3	10.2 ± 4.7
1633+382	B	8	1.5 ± 0.0	−86.2 ± 0.5	0.15 ± 0.03	−86.2 ± 3.0	11.4 ± 1.9	0.0 ± 3.1
1641+399	B	9	1.7 ± 0.0	−95.0 ± 0.6	0.49 ± 0.02	−99.9 ± 1.7	17.0 ± 0.8	5.0 ± 1.8
	C	5	0.9 ± 0.0	−100.6 ± 0.7	0.37 ± 0.03	−92.9 ± 2.5	12.9 ± 0.9	7.7 ± 2.6
1642+690	B	5	2.2 ± 0.1	−162.4 ± 1.6	0.38 ± 0.04	−161.0 ± 4.8	16.0 ± 1.6	1.4 ± 5.0
1655+077	B	5	3.7 ± 0.0	−38.4 ± 0.6	0.43 ± 0.03	−46.6 ± 3.4	15.4 ± 1.0	8.2 ± 3.5
	C	**5**	**8.0 ± 0.0**	**−44.2 ± 0.2**	**0.14 ± 0.02**	**17.1 ± 6.1**	**4.9 ± 0.9**	**61.3 ± 6.1**
1800+440	B	5	2.6 ± 0.1	−163.1 ± 1.4	0.49 ± 0.04	−155.7 ± 4.3	18.6 ± 1.6	7.4 ± 4.5
1845+797	**B**	**9**	**5.5 ± 0.0**	**−40.9 ± 0.3**	**0.55 ± 0.03**	**−29.9 ± 2.2**	**2.1 ± 0.1**	**10.9 ± 2.2**
	C	**10**	**7.2 ± 0.0**	**−36.0 ± 0.2**	**0.61 ± 0.02**	**−26.6 ± 1.0**	**2.3 ± 0.1**	**9.3 ± 1.0**
1928+738	B	8	2.1 ± 0.1	165.3 ± 0.7	0.29 ± 0.03	158.4 ± 3.2	5.6 ± 0.6	7.0 ± 3.3
1957+405	D	8	3.0 ± 0.0	−78.6 ± 0.2	0.18 ± 0.02	−78.2 ± 2.0	0.7 ± 0.1	0.4 ± 2.0
	E	8	2.2 ± 0.0	−79.7 ± 0.4	0.19 ± 0.03	−75.6 ± 3.1	0.7 ± 0.1	4.1 ± 3.1
	F	6	1.7 ± 0.1	−79.4 ± 0.5	0.22 ± 0.03	−79.5 ± 1.9	0.8 ± 0.1	0.1 ± 2.0
	G	8	1.2 ± 0.1	−79.0 ± 0.7	0.16 ± 0.03	−80.2 ± 2.9	0.6 ± 0.1	1.2 ± 2.9
2005+403	B	5	3.2 ± 0.1	119.8 ± 1.4	0.20 ± 0.03	83.6 ± 13.6	14.9 ± 2.1	36.2 ± 13.7
2113+293	**B**	**5**	**0.3 ± 0.0**	**177.0 ± 2.2**	**0.04 ± 0.01**	**−131.3 ± 8.2**	**2.4 ± 0.3**	**51.7 ± 8.5**
2145+067	**C**	**8**	**0.6 ± 0.0**	**−119.4 ± 0.7**	**0.03 ± 0.01**	**−156.4 ± 5.3**	**1.8 ± 0.3**	**37.0 ± 5.3**

TABLE 3—*Continued*

Object (1)	Component (2)	N (3)	$\langle R \rangle$ (mas) (4)	$\langle \vartheta \rangle$ (deg) (5)	μ (mas yr^{-1}) (6)	ϕ (deg) (7)	$\beta_{\rm app}$ (8)	$\lvert\langle \vartheta \rangle - \phi\rvert$ (deg) (9)
2200+420	B	7	2.4 ± 0.1	-171.6 ± 1.6	1.41 ± 0.12	-170.7 ± 3.1	6.5 ± 0.6	0.9 ± 3.5
	C	**5**	$\mathbf{2.5 \pm 0.2}$	$\mathbf{-171.4 \pm 1.5}$	$\mathbf{1.16 \pm 0.22}$	$\mathbf{172.8 \pm 3.4}$	$\mathbf{5.3 \pm 1.0}$	$\mathbf{15.8 \pm 3.7}$
2201+315	B	6	2.8 ± 0.0	-144.5 ± 1.2	0.34 ± 0.03	-142.7 ± 5.3	6.3 ± 0.5	1.8 ± 5.4
2223−052	B	6	1.9 ± 0.1	102.4 ± 2.8	0.50 ± 0.08	107.3 ± 6.4	32.9 ± 5.4	4.9 ± 7.0
	C	7	5.2 ± 0.1	98.0 ± 0.3	0.31 ± 0.03	90.6 ± 3.3	20.6 ± 1.8	7.4 ± 3.3

NOTES.—Sources with significant nonradial motion are shown in bold print. Col. (1): IAU name (B1950.0). Col. (2): Component identifier. Col. (3): Number of epochs with measured position. Col. (4): Mean radial position, relative to the core. Col. (5): Mean structural position angle, relative to the core. Col. (6): Angular velocity. Col. (7): Direction of velocity. Col. (8): Linear speed in units of the speed of light. Col. (9): Misalignment angle.

components move in opposite directions from the core with a velocity, $\beta \sim 0.26$, that is only mildly relativistic. Plots of component position versus time for all of the two-sided jets are shown in Figure 2. For most of these sources we were able to identify the central component at each epoch and so determine the motion of individual features away from the center. In a few cases, however, such as 1404+286 (epochs 1998.83 and 1999.55), the central core was not detected at one or more epochs, either because it was weak or because the dynamic range was limited for that observation. In these cases we have interpolated from the positions of the outer features, to find the "virtual" center, and we have used that to determine the motion of the individual outer features. For the source 1323+321 even that procedure was not possible since the structure appears to be two-sided, but we do not see the core at any epoch. Moreover, our imaging of this source is not completely satisfactory as a result of its large angular size and the limited interferometer spacings sampled by our data.

4.2.5. *Peaked Spectrum Sources*

GPS sources are characterized by their sharp low-frequency cutoff and general absence of prominent large-scale structure. There is no consensus as to whether the observed spectral cutoff in these sources is due to synchrotron self-absorption or free-free absorption (Shaffer et al. 1999). Previous VLBI observations have suggested that GPS sources have a simple double-structure morphology with little or no significant motions (e.g., O'Dea 1998). Thirteen of our sources are classified as GPS sources, of which we, so far, have observations of eight at three or more epochs. Of these, only 1345+125 shows superluminal motion. The mean velocity observed for the GPS sources in our sample is only $(0.5 \pm 1.5)c$. None of the GPS sources have $\beta_{\rm app} > 1.5$.

The existence of a sharp peak in the spectra of these sources implies that the individual components each peak up at about the same frequency. This means that the different components probably have comparable Doppler shifts, and if the spectral cutoff is due to synchrotron self-absorption, they should have comparable brightness temperatures. Some GPS sources, such as 0552+398 and 0642+449, contain a single unresolved strong component, and so an interpretation in terms of synchrotron self-absorption is required for any reasonable magnetic field strength. However, for other GPS sources we note the very different appearance of the core and jet components; nevertheless, they have a common cutoff frequency. Moreover, many of the peaked spectrum sources included in our study have sharply bent jet structure suggesting very different amounts of Doppler boosting and frequency shift of the self-absorption peak. Free-free absorption probably plays an important role in determining the spectra of these sources. Since many of the core-jet GPS sources show little or no motion, we suggest that possibly the jet flow in these sources is nonrelativistic or that these sources are seen at very large viewing angles, rather than that the measured velocity is the advance speed of a young double-lobe radio galaxy as suggested by Owsianik & Conway (1998). Either of these scenarios would imply a small Doppler shift. GPS sources do not have any extended double-lobe structure, which may be a consequence of the slow jets that do not carry sufficient energy to form extended radio lobes.

We note that in some cases, such as CTA 102, which had a peaked spectrum in the past, there are large variations in the total flux density (Kovalev et al. 2002), which probably reflects significant relativistic boosting. Lister (2003) and Kovalev (2004) have argued that these sources are not bona fide GPS sources but "masquerading blazars" that often contain bright transient jet features that dominate their radio spectrum.

4.2.6. *Sources with Extended Double Structure*

As a result of our selection criteria, most of the sources included in our study are dominated by their flat-spectrum compact structure; they are mostly identified with quasars. Some quasars, however, also have extended structure with relatively steep radio spectra, in addition to their flat-spectrum compact core. We have included a few of these lobe-dominated sources in our study, although they did not meet our selection criteria. Extended structure is more common among the active galaxies. The following sources in Table 2 have significant double-lobe steep-spectrum extended structure: NGC 315 (0055+300), NGC 1052 (0238−084), 3C 111 (0415+379), 3C 120 (0430+052), M87 (1228+126), 3C 390.3 (1845+797), and Cygnus A (1945+405). All are identified with galaxies containing a relatively strong AGN. All but NGC 1052 and 3C 120 are dominated by the extended steep-spectrum double-lobe structure even at 15 GHz. In the framework of standard relativistic beaming models, radio galaxies and lobe-dominated sources are presumed to lie close to the plane of the sky and thus should show values of $\beta_{\rm app} \sim 1$. However, 3C 111, 3C 120, and 3C 390.3 each show rather large apparent motions, and it is not clear how they fit into standard unification models.

These objects are all broad-line radio galaxies (BLRGs), although 3C 120 has also been classified as a narrow-line radio galaxy (NLRG). The NLRGs are thought to lie at rather large angles to the line of sight, and polarimetry shows that in some cases they contain a central quasar and a broad-line region that are hidden by a dusty torus. The NLRGs do not show strong superluminal motion. Sources 3C 111, 3C 120, and 3C 390.3 do show superluminal motion and hence must

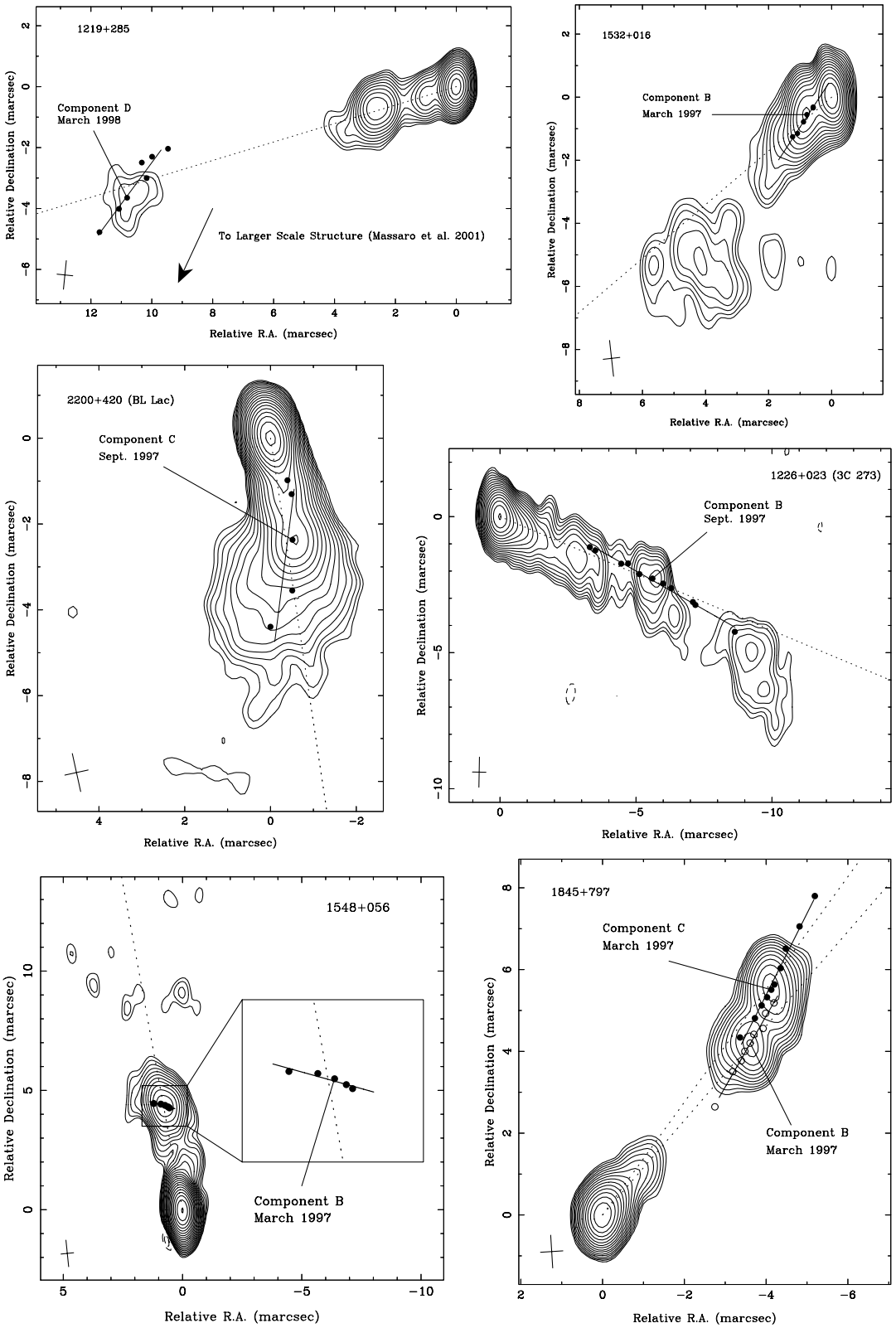

FIG. 7.—Selected images of sources with jets that show nonballistic component motion. Measured component positions for each epoch are superimposed on the images along with the vector motion (*solid lines*) in the right ascension–declination plane. Dashed lines represent the mean structural position angles, $\langle\vartheta\rangle$, for each component.

be at small angles to the line of sight (less than about 11° for 3C 111). The BLRGs are not well understood, and they may have a wide range of intrinsic luminosity and orientation (Dennett-Thorpe et al. 2000).

On the other hand, the jets of other lobe-dominated sources appear to be subrelativistic. The powerful radio galaxy Cygnus A contains twin jets pointed toward the distant hot spots. The approaching and receding jets appear to propagate with velocities of $0.7c$ and $0.2c$, respectively, and we find relatively slow speeds of $(0.16 \pm 0.03)c$ in the parsec-scale jet of NGC 315. In the case of the radio galaxy NGC 1052, we have reported a two-sided flow with subrelativistic jet speeds of only $0.26c$ (Vermeulen et al. 2003b) on both sides of the core. At least in these radio galaxies, the intrinsic jet flow close to the core appears to have only moderate speeds with $\beta_{\rm app} \ll 1$. Thus, it appears that the observed distribution of speeds and/or degree of jet asymmetry cannot be interpreted simply in terms of the orientation of a twin relativistic jet with $\beta \sim 1$, unless the observed speeds do not reflect the actual jet flow speed, or the radiation from a high-speed inner spine is not observed as a result of a more slowly moving outer sheath that dominates the emission at large angles from the jet direction. As we show in § 4.4.1, highly relativistic jets are relatively rare among the general population of radio jets.

4.2.7. *Comparison with Other Velocity Studies*

Other recent VLBA monitoring observations (e.g., Jorstad et al. 2001a, 2001b; Britzen et al. 2001; Homan et al. 2001; Vermeulen et al. 2003a) made at other wavelengths with different resolution and with different sampling intervals are complementary to our observations and may be used to extend the range of size and timescales over which jet kinematics may be studied.

Jorstad et al. (2001a, 2001b) have used the VLBA to study the motions in a sample of strong sources at 7 and 13 mm. These observations probe the source structure and motions on a scale about 3 times smaller than our 2 cm observations, but as a result of the decreased surface brightness at 7 mm, they are generally not able to trace the motions beyond a few milliarcseconds from the core. From the comparison of the observed motions for the sources in common to our two studies, it is possible to trace the motions of individual components over a wider range of scales than is possible from either set of observations alone.

We have compared our velocities determined at 15 GHz with those of Jorstad et al. (2001a, 2001b). There appears to be little agreement in the individual source speeds found by the two studies. On average, the Jorstad et al. (2001a, 2001b) speeds appear systematically higher, possibly because their observations were carried out at shorter wavelengths and probed jet regions closer to the core.

Britzen et al. (1999, 2001) and Vermeulen et al. (2003a) have discussed jet motions in a large sample of sources at 6 cm, taken from the Caltech-Jodrell CJ surveys covering declinations greater than +35°. These observations have lower angular resolution than ours and are thus more sensitive to the lower surface brightness structure located downstream. Vermeulen et al. (2003a) quote a mean velocity for quasar and galaxy jets of $2.9c$ and $0.9c$, respectively. This appears to be less than the values of $(7.3 \pm 0.8)c$ and $(1.7 \pm 0.8)c$ that we measure at 2 cm for the brightest features in each source. On the other hand, Jorstad et al. (2001b), working primarily at 0.7 and 1.3 cm, find systematically faster velocities in those sources where our samples overlap. These results suggest that there is a systematic decrease in $\beta_{\rm app}$ with increasing wavelength, probably because the observations at different wavelengths sample different parts of jet structure. In a separate paper (R. C. Vermeulen et al. 2004, in preparation) we will discuss, in more detail, the motions of those sources in common to the 6 and 2 cm samples.

4.3. *Implications for Relativistic Beaming Models*

4.3.1. *Ballistic Models*

The simplest model to consider is a pure ballistic model with a common flow velocity for all sources, with $\beta_p = \beta_b \sim 1$, and a flow that is intrinsically symmetric. In this simple case, observations of the apparent velocities, as well as the ratio of flux densities of approaching and receding components, can, in principle, be used to solve uniquely for γ and θ and thus provide a test of the hypothesis that $\beta_p = \beta_b$. However, even early VLBI data indicated that this simple model is not tenable (Vermeulen & Cohen 1994; Lister & Marscher 1997).

In a flux density–limited sample, the combined effect of available solid angle and Doppler boosting leads to a distribution of $\beta_{\rm app}$ with many values close to γ (Vermeulen & Cohen 1994). On the other hand, if Doppler boosting is not an important selection mechanism, then in most cases $\beta_{\rm app} \sim 1$. Figure 3 shows the expected distribution of apparent velocities for the case in which $\gamma_p = \gamma_b$ (see § 4.1) along with the corresponding distribution for a randomly oriented sample. None of the distributions shown in Figure 4 or Figure 5 are consistent with either of these simple ballistic models as there is neither evidence of the peak at $\beta_{\rm app} \sim \gamma$ characteristic of the simple Doppler boosted models nor evidence of the sharp low-speed cutoff at $\beta_{\rm app} \sim 1$ characteristic of models that ignore Doppler boosting.

How do we reconcile the difference between the observed and predicted distributions? There must be either a spread in intrinsic velocity (e.g., Lister & Marscher 1997) or a difference between the bulk flow velocity and the pattern velocity, so that there is less Doppler bias in favor of observing beams that are oriented close to the critical angle (Vermeulen & Cohen 1994). In Figure 3 we plot a model with a spread of intrinsic velocity such that $n(\gamma) \propto \gamma^{-1.5}$. This model has equal pattern and bulk velocities and reproduces the general characteristics of the observed distribution of superluminal speeds. A more detailed analysis will be discussed by M. L. Lister et al. (2004, in preparation).

4.3.2. *Randomly Oriented Samples*

Based on earlier observations of apparent velocity distributions, Ekers & Liang (1990) suggested that the simple model with no Doppler bias provided an adequate fit to the observed distributions of $\beta_{\rm app}$ with only a slight adjustment needed, which was satisfied by introducing an obscuring torus. However, comparison of our data with models that do not include Doppler boosting shows poor agreement, since, as shown in Figure 3, in the absence of Doppler boosting, most sources are expected to lie close to the plane of the sky where $\beta_{\rm app} \sim 1$. This appears to be inconsistent with the tail of the velocity distribution that we find extending toward larger apparent velocities. Following the discussion of Cohen (1990), a detailed analysis of the observed velocities shows that the probability of the sources having been picked at random from a parent population that is isotropically distributed is less than

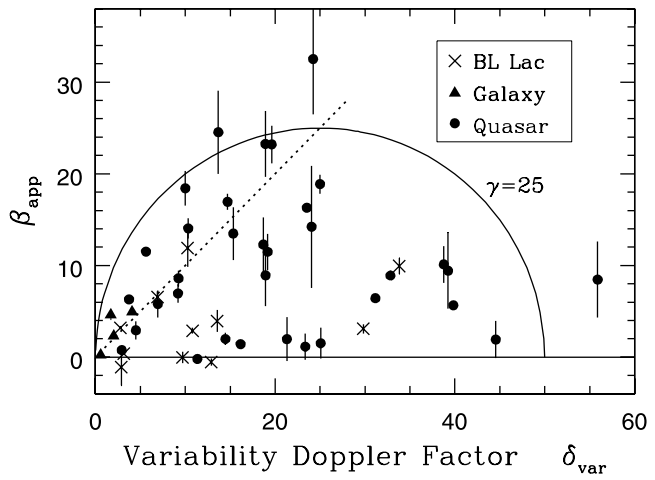

FIG. 8.—Apparent velocity, $\beta_{\rm app}$, plotted against variability Doppler factor, $\delta_{\rm var}$, for the fastest component found in 49 sources calculated using the method of Lähteenmäki & Valtaoja (1999) with an intrinsic brightness temperature $T_b^{\rm int} = 2 \times 10^{10}$ K. The solid line shows the expected locus of points for Lorentz factor values of 25. The dotted line represents the $1/\gamma$ cone where $\delta_{\rm var} = \beta_{\rm app}$.

10^{-5}. We therefore conclude that the sources are preferentially aligned along the line of sight, as would be expected if Doppler boosting is in fact important.

4.4. *Comparison with Other Relativistic Velocity Indicators*

While the actual observation of superluminal motion in radio source jets remains the most direct way of establishing the existence of relativistic motion, comparison of the observed values of $\beta_{\rm app}$ with other velocity indicators also provides important tests of beaming models and specifically the relation between pattern and bulk flow speeds. This includes flux density variability (Hughes et al. 1992; Lähteenmäki & Valtaoja 1999; Lähteenmäki et al. 1999), maximum brightness temperature (Kellermann & Pauliny-Toth 1969; Readhead 1994; Guijosa & Daly 1996), the ratio of core to extended radio luminosity (Orr & Browne 1982), the gamma-ray luminosity (von Montigny et al. 1995; Hartman et al. 1999; Mattox et al. 1997, 2001), or observations of inverse Compton X-rays (Ghisellini et al. 1993). Relativistic boosting also affects the radio source counts and luminosity functions (Padovani & Urry 1992; Wall & Jackson 1997), which provide a consistency check on beaming models.

4.4.1. *Relation between Observed Velocity and Flux Density Variations*

Flux density changes are commonly seen in superluminal sources, and their short timescale is generally taken to imply high brightness temperatures. The variability timescale and the timescale for apparent transverse motion are both compressed as a result of the forward motion; hence, we might expect to see a relation between $\beta_{\rm app}$ and the flux density variability provided that β_b is related to β_p. Lähteenmäki & Valtaoja (1999) used variability data at 1.3 cm and 8 mm from the Metsähovi Observatory to calculate a variability Doppler factor, $\delta_{\rm var}$, assuming an intrinsic brightness temperature characteristic of a self-absorbed synchrotron source in which the particle and magnetic energy are in equilibrium. We have recalculated their values using the cosmology given in § 1 and for different values of intrinsic brightness temperature. Since $\delta_{\rm var}$ varies inversely as the cube root of the assumed intrinsic temperature in the synchrotron plasma, $T_b^{\rm int}$, $\delta_{\rm var}$ is relatively insensitive to the assumed value of $T_b^{\rm int}$.

In Figure 8 we plot $\beta_{\rm app}$ against $\delta_{\rm var}$ for the 49 sources in common to the Metsähovi and VLBA samples. We calculate $\delta_{\rm var} = (T_b^{\rm var}/T_b^{\rm int})^{1/3}$ assuming a spectral index of zero and where $T_b^{\rm var}$ is the apparent brightness temperature calculated from the variability timescale, by assuming that it is limited by the size of the source divided by the speed of light. Five sources that only have components located at a bend in the jet were excluded, as they probably reflect a standing shock wave, or perhaps a stationary location in a helical jet where the flow is closest to the line of sight and hence is boosted most strongly. In either case the measured velocity is a poor indicator of the flow velocity and not relevant in discussing relativistic effects. The sample we use contains five active galaxies, 14 BL Lac objects, and 30 quasars. Most points lie inside the "$1/\gamma$ cone" ($\beta_{\rm app} = \delta_{\rm var}$) as they should for a flux density–limited sample (Vermeulen & Cohen 1994).

Cohen et al. (2003) have compared Figure 8 with the results of a simulation generated by randomly picking a flux-limited sample from an isotropically distributed population with power-law distributions of luminosity and γ and for several values of $T_b^{\rm int}$ over the range 4×10^9–1×10^{11} K. The value $T_b^{\rm int} \sim 2 \times 10^{10}$ K gives the best fit between the measured and simulated data. However, although there does appear to be an upper limit to $\beta_{\rm app}$ that is close to the expected locus for components with $\gamma = 25$, the detailed distribution is not well matched to that expected from the simulation (Lister & Marscher 1997).

Calculations of the variability Doppler factor using values of $T_b^{\rm int}$ closer to the inverse Compton limit, $\sim 10^{12}$ K, lead to distributions on the $\beta_{\rm app}$-$\delta_{\rm var}$ plane that are very different from those expected from the simulations. We conclude that $T_b^{\rm int}$ is perhaps an order of magnitude below the inverse Compton limit.

For this application, we have used the *fastest* feature for each source, on the grounds that these velocities should be more representative of the true flow velocities. Slower moving components, especially those located at a bend in the jet, may be dominated by standing shock waves. Forward shock waves might also exist, and trying to understand their role is a goal of our study. Other geometries have been suggested for the jet, including a fast "spine," which we would preferentially see, surrounded by a slower shell. In this case, the spine would probably also control the flux variations, so that using the fastest (spine) velocity for $\beta_{\rm app}$ is appropriate.

We have also examined values of $\delta_{\rm var}$ calculated from the UMRAO database at our wavelength of 2 cm and noted a large dispersion between Doppler factors deduced from these data and the shorter wavelength Metsähovi data. Thus, the robustness of the Doppler factors calculated in this way appears to be uncertain. The Michigan data cover a longer time span but are at longer wavelengths where individual outbursts appear to overlap in time.

The Lorentz factor γ in a superluminal jet is important because it is intrinsic to the jet, whereas $\beta_{\rm app}$ and $\delta_{\rm var}$ are the observables that depend on the jet orientation. The distribution of γ may give information on the physics of the collimation region. From the values of $\beta_{\rm app}$ and δ shown in Figure 8 we calculate the actual Lorentz factors, shown as a histogram in Figure 9. We believe that the apparent deficit in the first bin of Figure 9 for the quasars may be a selection effect or just due to small number statistics. To be fully consistent with the analysis above and the choice $T_b^{\rm int} = 2 \times 10^{10}$ K, the Lorentz

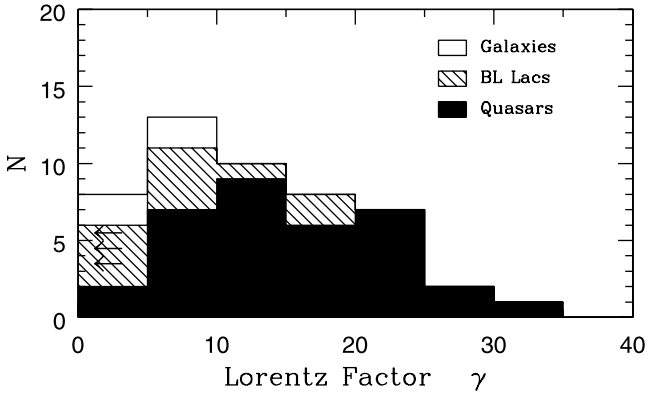

FIG. 9.—Histogram of Lorentz factors for 49 sources, calculated from $\beta_{\rm app}$ and $\delta_{\rm var}$ based on $T_b^{\rm int} = 2 \times 10^{10}$ K.

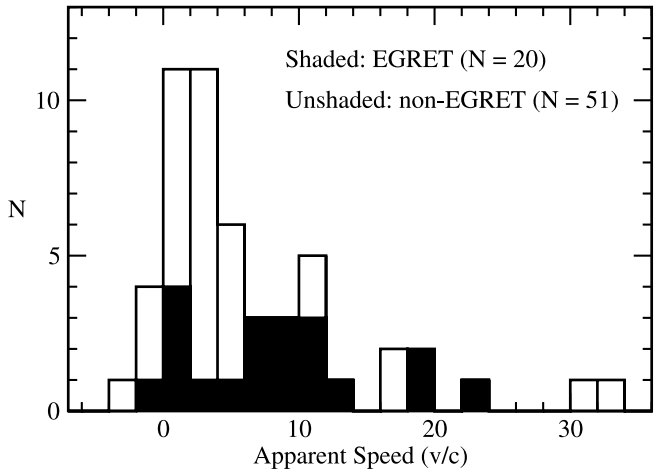

FIG. 10.—Histogram of the brightest component speed in EGRET-detected and non–EGRET-detected sources for our representative flux density–limited sample.

factors should have a power-law distribution. However, the number of objects is too small and the errors too uncertain to make a meaningful comparison. A small Lorentz factor implies a low velocity and small flux density variations, and the latter especially is less likely to be measurable. However, the calculated Lorentz factors are useful in showing that there must be a wide range of γ in the superluminal sources. The galaxies all have rather low Lorentz factors, while the quasars have a broad distribution up to $\gamma \approx 30$.

4.4.2. *Gamma-Ray Sources*

Many of the sources included in our study have been cataloged as strong gamma-ray sources according to measurements made by the EGRET detector on board the *Compton Gamma Ray Observatory* (von Montigny et al. 1995; Hartman et al. 1999; Mattox et al. 1997, 2001; Sowards-Emmerd et al. 2003). It is generally thought that the gamma-ray emission occurs deep within the relativistic jet. Arguments based on size limits deduced from time variability and the cross section for pair production suggest that the gamma-ray emission, like the radio emission, is Doppler boosted (Dermer & Schlickeiser 1994). In fact, the gamma rays may be even more strongly beamed than the radio emission since the former generally have a steeper spectral index, α, and the flux density boosting varies as $\delta^{(2-\alpha)}$ for continuous jets. Furthermore, Dermer (1995) has shown that if the bulk of the gamma rays are produced by external Compton scattering off photons associated with the accretion disk, the resulting gamma-ray emission will be boosted by an additional factor of $\delta^{(1-\alpha)}$.

If gamma-ray–loud AGNs do indeed have systematically high Doppler factors, then we might expect to see a different apparent speed distribution for them than for AGNs that have not been detected in gamma rays. The situation is complicated by the possibility that the gamma-ray–loud jets may be seen inside the critical angle for maximizing superluminal motion ($1/\gamma$) and therefore might have slow apparent projected speeds. However, Monte Carlo simulations based on a simple linear relationship between radio and gamma-ray luminosity (e.g., Lister & Marscher 1999; Lister 1999) confirm that in a flux density–limited radio sample, AGNs detected by EGRET should have typically higher speeds than those that were not detected in gamma rays.

Jorstad et al. (2001b) recently measured the apparent speeds of 33 EGRET-detected AGNs. They found a mean value of 16c for the fastest component in each source and concluded that the gamma-ray sources have larger Lorentz factors than the general population of radio sources. However, Jorstad et al. (2001b) did not have a non–gamma-ray control sample observed in the same way and at the same wavelength with which to compare their results.

We have classified our sample into EGRET and non-EGRET sources based on the list of Mattox et al. (2001) and recently modified by Sowards-Emmerd et al. (2003). These authors classify gamma-ray sources from the third EGRET catalog (Hartman et al. 1999) as "highly probable" and "plausible" AGN identifications, based on Bayesian statistics and their proximity to bright flat-spectrum radio sources. In Figure 10 we show the distribution of measured speeds for the EGRET-detected and nondetected sources. For the brightest jet component found in the 18 EGRET sources in our representative sample we found a median speed of $(8.0 \pm 1.6)c$ compared with a value of $(3.9 \pm 1.1)c$ for the 53 sources with no EGRET detections. A K-S test suggests that the difference appears significant at the 90% level. For the purpose of this analysis we have included the two "plausible" EGRET sources, 2230+114 and 1156+295, as detections. Reclassifying them as nondetections had no effect on our results, and neither did excluding the sources with negative velocities from our analysis.

These results are consistent with the idea that the radio emission from gamma-ray quasars is indeed more strongly beamed than for the whole radio quasar population. However, our samples are incomplete and may therefore be biased.

4.5. *The Angular Velocity–Redshift Relation*

Figure 11 shows the measured values of angular velocity μ versus redshift for the fastest E or G rated component found in the sources in Table 2. The line represents $\mu_{\rm max}$, the fastest proper motion a source can display if it has $\gamma = 25$. The variables are the observables, uncontaminated by modeling, and hence are of value in showing directly that (1) at all redshifts, the observed velocities are not clustered near the maximum value as expected from the simple ballistic models with a single Lorentz factor for all sources, (2) low values of μ are seen at all z, and (3) high values of μ are seen only at low z. This is true for galaxies, BL Lac objects, and quasars and appears inconsistent with noncosmological interpretation of quasar redshifts as proposed by Burbidge (2004).

An early version of this plot (Cohen et al. 1988) was used to show that the standard paradigm for superluminal motion provided a crude upper bound to the points in Figure 11 and

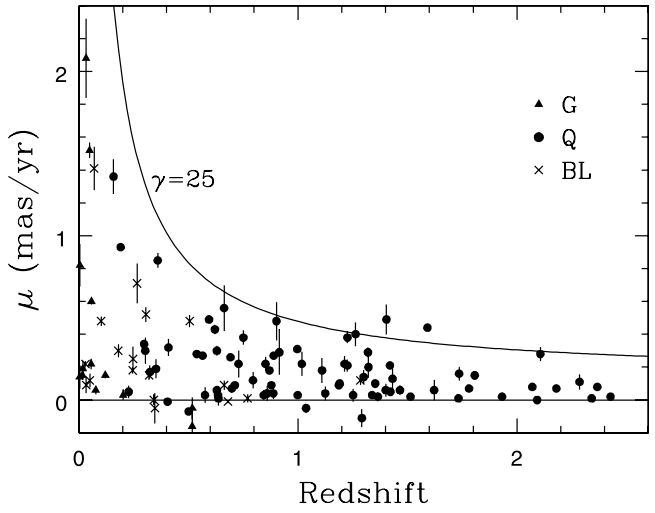

FIG. 11.—The μ-z diagram showing the distribution of angular velocity for the fastest component of the 110 sources that has a quality factor of G or E. The solid line is the maximum value of $\beta_{\rm app}$ for $\gamma = 25$.

that the maximum value of $\beta_{\rm app}$ in 32 sources was about 13 ($H_0 = 70$, $q_0 = 0.5$). The $\mu_{\rm max}$ line in Figure 11 is, similarly, a crude upper bound to the measured points and shows that $\beta_{\rm app,\,max} \sim 25$. Note that the cosmology used in this paper makes $\beta_{\rm app}$ somewhat larger than for a cosmology with $\Omega_m = 1$ and $\Omega_\Lambda = 0$.

The data in Cohen et al. (1988) were compiled at assorted frequencies, mostly below 15 GHz, and corresponded to measurements made at different distances from the core, which may explain the difference in $\beta_{\rm app,\,max}$. As we have discussed in § 4.2.7, there is some evidence that observations at high frequencies give higher values of μ than observations at lower frequencies.

Vermeulen & Cohen (1994) and Lister & Marscher (1997) have shown that if Doppler boosting is important, then even rather small samples of superluminal sources will show $\beta_{\rm app,\,max}$ near the maximum value of the distribution of γ, $\gamma_{\rm max}$. Hence, we expect that $\gamma_{\rm max} \sim 25$ for the sample shown in Figure 11. This is marginally consistent with Figure 9, reflecting that Lorentz factors calculated according to the method in § 4.4.1 have rather large uncertainties.

5. SUMMARY

We have studied the kinematics of a large well-defined sample of 110 quasar and active galaxy jets and find a distribution of apparent velocities typically between 0 and 14c but ranging up to about 34c. There is evidence of a characteristic velocity in each jet that may represent the true plasma flow velocity. We have found that quasar jets generally have larger apparent velocities than jets associated with BL Lac objects and active galaxies, although the distributions overlap. Our measured values of $\beta_{\rm app}$ are consistent with the Doppler factors, $\delta_{\rm var}$, calculated from time variability and a parent population having a steep power-law distribution of intrinsic Lorentz factors extending down to moderate velocities and an intrinsic brightness temperature close to 2×10^{10} K. This is close to the value expected if the particle and magnetic energy densities in the jet are comparable (Readhead 1994; Singal & Gopal-Krishna 1985).

In approximately one-third of the well-studied jets, we find evidence of nonballistic motion; that is, the flow is not along the direction away from the core. In most of the jets, we find no deviation from a constant speed, but in a few sources, we do see evidence of changes in speed and direction of individual features. Mostly, the flow appears to lie along the direction of the local jet orientation. However, in some cases the flow has a significant nonradial component, which points toward more distant parts of the jet. This suggests that there is a continuous flow along a preexisting channel. Contrary to the assumption of the simple unified models, in some jets, the intrinsic flow appears to be with speeds much less than c.

Observations made at higher frequencies sample jet features located closer to the core, and they typically show larger apparent velocities than we observe at 15 GHz, while lower frequency observations show yet smaller speeds. Sources with stable GPS spectra show little or no motion; the jet flow in these sources may be nonrelativistic or lie in the plane of the sky with a correspondingly small Doppler shift.

We find that jets of quasars that have been observed as strong gamma-ray sources have marginally higher speeds than those that are not gamma-ray sources. This is consistent with models where the gamma-ray sources have more highly relativistic jets and are aligned closer to the line of sight. However, our analysis is limited by both small number statistics and the uncertainties in the ever-changing analysis of the EGRET catalogs. In addition, with the limited range of flux density observed by EGRET, there is no well-defined class of gamma-ray–loud and gamma-ray–quiet sources analogous to the radio-loud and radio-quiet classifications. More sensitive observations with the next generation of gamma-ray observatories, such as *GLAST*, combined with jet speed data for our complete radio sample of 133 radio sources, should be very useful for investigating gamma-ray production mechanisms in AGN jets and relating the gamma-ray properties to the observed jet outflow.

E. Ros et al. (2004, in preparation) have extended these observations and analysis through 2001 and 2002. M. L. Lister et al. (2004, in preparation) have defined a more complete sample of 133 sources and are continuing the observations of these sources including linear and circular polarization (D. C. Homan et al. 2004, in preparation). Observations with this new sample will allow a more robust comparison with models, a better estimate of the distribution of intrinsic Lorentz factors, and a start to understanding the evolution of jet magnetic fields.

The VLBA is a facility of the National Radio Astronomy Observatory, which is operated by Associated Universities, Inc., under a cooperative agreement with the National Science Foundation. We thank Hugh and Margo Aller and Tigran Arshakian for many valuable discussions, Mike Russo, Andrew West, and John Armstrong for their help with the data analysis, and the NRAO staff for their support in the data acquisition and correlation. We also thank the referee for his very constructive suggestions, which have helped to clarify our presentation. Ed Fomalont and Leonid Gurvits kindly allowed us to use their 1998 and 1999 images to supplement our own observations during that period. We have made use of the database from the UMRAO, which is supported by funds from the University of Michigan, and additional VLBA observations of Cygnus A by Uwe Bach to help interpret our own data for this source. Part of this work was done while R. C. V. held an appointment at Caltech. K. I. K. thanks Caltech and the MPIfR for their support and hospitality during several visits.

REFERENCES

Alef, W., Wu, S. Y., Preuss, E., Kellermann, K. I., & Qiu, Y. H. 1996, A&A, 308, 376
Aller, M. F., Aller, H. D., & Hughes, P. A. 1992, ApJ, 399, 16
———. 2003, in ASP Conf. Ser. 300, Radio Astronomy at the Fringe, ed. J. A. Zensus, M. H. Cohen, & E. Ros (San Francisco: ASP), 159
Barthel, P. D. 1989, ApJ, 336, 606
Beasley, A. J., Gordon, D., Peck, A. B., Petrov, L., MacMillan, D. S., Fomalont, E. B., & Ma, C. 2002, ApJS, 141, 13
Bennett, C. L., et al. 2003, ApJS, 148, 97
Blandford, R. D., & Königl, A. 1979, ApJ, 232, 34
Blandford, R. D., & Rees, M. J. 1974, MNRAS, 169, 395
Britzen, S., Vermeulen, R. C., Taylor, G. B., Campbell, R. M., Browne, I. W. A., Wilkinson, P. N., Pearson, T. J., & Readhead, A. C. S. 2001, in IAU Symp. 205, Galaxies and Their Constituents at the Highest Angular Resolutions, ed. R. T. Schilizzi, S. Vogel, F. Paresce, & M. Elvis (San Francisco: ASP), 106
Britzen, S., Vermeulen, R. C., Taylor, G. B., Pearson, T. J., Readhead, A. C. S., Wilkinson, P. N., & Browne, I. W. A. 1999, in ASP Conf. Ser. 159, BL Lac Phenomenon, ed. L. O. Takalo & A. Sillanpää (San Francisco: ASP), 431
Burbidge, G. 2004, ApJ, 603, 28
Carangelo, N., Falomo, R., Kotilainen, J., Treves, A., & Ulrich, M.-H. 2003, A&A, 412, 651
Cohen, M. H. 1990, in Parsec-scale Radio Jets, ed. J. A. Zensus & T. J. Pearson (Cambridge: Cambridge Univ. Press), 317
Cohen, M. H., Barthel, P. D., Pearson, T. J., & Zensus, J. A. 1988, ApJ, 329, 1
Cohen, M. H., Cannon, W., Purcell, G. H., Shaffer, D. B., Broderick, J. J., Kellermann, K. I., & Jauncey, D. L. 1971, ApJ, 170, 207
Cohen, M. H., et al. 1977, Nature, 268, 405
———. 2003, in ASP Conf. Ser. 300, Radio Astronomy at the Fringe, ed. J. A. Zensus, M. H. Cohen, & E. Ros (San Francisco: ASP), 27
Dallacasa, D., Stanghellini, C., Centonza, M., & Fanti, R. 2000, A&A, 363, 887
Dennett-Thorpe, J., Barthel, P. D., & van Bemmel, I. M. 2000, A&A, 364, 501
Dent, W. A. 1965, Science, 148, 1458
———. 1972, Science, 175, 1105
Dermer, C. D. 1995, ApJ, 446, L63
Dermer, C. D., & Schlickeiser, R. 1994, ApJS, 90, 945
de Vries, W. H., Barthel, P. D., & O'Dea, C. P. 1997, A&A, 321, 105
Ekers, R., & Liang, H. 1990, in Parsec-scale Radio Jets, ed. J. A. Zensus, & T. J. Pearson (Cambridge: Cambridge Univ. Press), 333
Ghisellini, G., Padovani, P., Celotti, A., & Maraschi, L. 1993, ApJ, 407, 65
Guijosa, A., & Daly, R. A. 1996, ApJ, 461, 600
Hartman, R. C., et al. 1999, ApJS, 123, 79
Hirabayashi, H., et al. 1998, Science, 281, 1825
Homan, D. C., Lister, M. L., Kellermann, K. I., Cohen, M. C., Ros, E., Zensus, J. A., Kadler, M., & Vermeulen, R. C. 2003, ApJ, 589, L9
Homan, D. C., Ojha, R., Wardle, J. F. C., Roberts, D. H., Aller, M. F., Aller, H. D., & Hughes, P. A. 2001, ApJ, 549, 840
Hoyle, F., Burbidge, G. R., & Sargent, W. 1966, Nature, 209, 751
Hughes, P. A., Aller, H. D., & Aller, M. F. 1992, ApJ, 396, 469
Istomin, Y. N., & Pariev, V. I. 1996, MNRAS, 281, 1
Jorstad, S. G., Marscher, A. P., Mattox, J. R., Aller, M. F., Aller, H. D., Wehrle, A. E., & Bloom, S. D. 2001a, ApJ, 556, 738
Jorstad, S. G., Marscher, A. P., Mattox, J. R., Wehrle, A. E., Bloom, S. D., & Yurchenko, A. V. 2001b, ApJS, 134, 181
Kellermann, K. I. 2002, Publ. Astron. Soc. Australia, 19, 77
Kellermann, K. I., & Pauliny-Toth, I. I. K. 1969, ApJ, 155, L71
Kellermann, K. I., Vermeulen, R. C., Zensus, J. A., & Cohen, M. H. 1998, AJ, 115, 1295 (Paper I)
———. 2000, in Astrophysical Phenomena Revealed by Space VLBI, ed. H. Hirabayashi, P. G. Edwards, & D. W. Murphy (Sagamihara: ISAS), 159
Kellermann, K. I., et al. 1999, NewA Rev., 43, 757
———. 2003, in ASP Conf. Ser. 299, High Energy Blazar Astronomy, ed. L. O. Takalo & E. Valtaoja (San Francisco: ASP), 117
Kovalev, Y. Y. 2003, in ASP Conf. Ser. 300, Radio Astronomy at the Fringe, ed. J. A. Zensus, M. H. Cohen, & E. Ros (San Francisco: ASP), 65
———. 2004, Baltic Astron., in press
Kovalev, Y. Y., Kovalev, Yu. A., Nizhelsky, N. A., & Bogdantsov, A. V. 2002, Publ. Astron. Soc. Australia, 19, 83
Kovalev, Y. Y., Nizhelsky, N. A., Kovalev, Y. A., Berlin, A. B., Zhekanis, G. V., Mingaliev, M. G., & Bogdantsov, A. V. 1999, A&AS, 139, 545
Kühr, H., Witzel, A., Pauliny-Toth, I. I. K., & Nauber, U. 1981, A&AS, 45, 367
Lähteenmäki, A., & Valtaoja, E. 1999, ApJ, 521, 493
Lähteenmäki, A., Valtaoja, E., & Wiik, K. 1999, ApJ, 511, 112
Lawrence, C. L. 1996, in IAU Symp. 173, Astrophysical Applications of Gravitational Lensing, ed. C. S. Kochanek & J. N. Hewitt (Dordrecht: Kluwer), 299
Lind, K. R., & Blandford, R. D. 1985, ApJ, 295, 358
Lister, M. L. 1999, Ph.D. thesis, Boston Univ.
———. 2001, ApJ, 562, 208
———. 2003, in ASP Conf. Ser. 300, Radio Astronomy at the Fringe, ed. J. A. Zensus, M. H. Cohen, & E. Ros (San Francisco: ASP), 71
Lister, M. L., Kellermann, K. I., & Pauliny-Toth, I. I. K. 2002, in Proc. of the 6th European VLBI Network Symp., ed. E. Ros, R. W. Porcas, A. P. Lobanov, & J. A. Zensus (Bonn: MPIfR), 135
Lister, M. L., Kellermann, K. I., Vermeulen, R. C., Cohen, M. H., Zensus, J. A., & Ros, E. 2003, ApJ, 584, 135
Lister, M. L., & Marscher, A. P. 1997, ApJ, 476, 572
———. 1999, Astropart. Phys., 11, 65
Mattox, J. R., Hartman, R. C., & Reimer, O. 2001, ApJS, 135, 155
Mattox, J. R., Schachter, J., Molnar, L., Hartman, R. C., & Patnaik, A. R. 1997, ApJ, 481, 95
O'Dea, C. P. 1998, PASP, 110, 493
Orr, M. J. L., & Browne, I. W. A. 1982, MNRAS, 200, 1067
Owsianik, I., & Conway, J. E. 1998, A&A, 337, 69
Padovani, P., & Urry, C. M. 1992, ApJ, 387, 449
Pauliny-Toth, I. I. K., & Kellermann, K. I. 1966, ApJ, 146, 634
Readhead, A. C. S. 1994, ApJ, 426, 51
Rees, M. J. 1966, Nature, 211, 468
———. 1967, MNRAS, 135, 345
Ros, E., Kellermann, K. I., Lister, M. L., Zensus, J. A., Cohen, M. H., Vermeulen, R. C., Kadler, M., & Homan, D. C. 2002, in Proc. of the 6th European VLBI Network Symp., ed. E. Ros, R. W. Porcas, A. P. Lobanov, & J. A. Zensus (Bonn: MPIfR), 105
Shaffer, D. B., Kellermann, K. I., & Cornwell, T. J. 1999, ApJ, 515, 558
Sholomitskii, G. B. 1965, AZh, 42, 673 (English transl. in Soviet Astron., 9, 516)
Singal, K. A., & Gopal-Krishna 1985, MNRAS, 215, 383
Sowards-Emmerd, D., Romani, R. W., & Michelson, P. F. 2003, ApJ, 590, 109
Stickel, M., Meisenheimer, K., & Kühr, H. 1994, A&AS, 105, 211
Stickel, M., Rieke, G. H., Kuehr, H., & Rieke, M. J. 1996, ApJ, 468, 556
Taylor, G. B., Vermeulen, R. C., Readhead, A. C. S., Pearson, T. J., Henstock, D. R., & Wilkinson, P. N. 1996, ApJS, 107, 37
Urry, C. M., & Padovani, P. 1995, PASP, 107, 803
Vermeulen, R. C. 1995, Proc. Natl. Acad. Sci., 92, 11385
Vermeulen, R. C., Britzen, S., Taylor, G. B., Pearson, T. J., Readhead, A. C. S., Wilkinson, P. N., & Browne, I. W. A. 2003a, in ASP Conf. Ser. 300, Radio Astronomy at the Fringe, ed. J. A. Zensus, M. H. Cohen, & E. Ros (San Francisco: ASP), 43
Vermeulen, R. C., & Cohen, M. H. 1994, ApJ, 430, 467
Vermeulen, R. C., Ros, E., Kellermann, K. I., Cohen, M. H., Zensus, J. A., & van Langevelde, H. J. 2003b, A&A, 401, 113
Véron-Cetty, M.-P., & Véron, P. 2001, A&A, 374, 92
von Montigny, C., et al. 1995, ApJ, 440, 525
Walker, R. C., Dhawan, V., Romney, J. D., Kellermann, K. I., & Vermeulen, R. C. 2000, ApJ, 530, 233
Wall, J. V., & Jackson, C. A. 1997, MNRAS, 290, L17
Whitney, A. R., et al. 1971, Science, 173, 225
Woltjer, L. 1966, ApJ, 146, 597
Zensus, J. A., Cohen, M. H., & Unwin, S. C. 1995, ApJ, 443, 35
Zensus, J. A., Ros, E., Kadler, M., Kellermann, K. I., Lister, M. L., Homan, D. C., Cohen, M. H., & Vermeulen, R. C. 2003, in ASP Conf. Ser. 300, Radio Astronomy at the Fringe, ed. J. A. Zensus, M. H. Cohen, & E. Ros (San Francisco: ASP), 27
Zensus, J. A., Ros, E., Kellermann, K. I., Cohen, M. H., & Vermeulen, R. C. 2002, AJ, 124, 662 (Paper II)